Gharyan Journal of Technolgy

Gharyan Journal of Technology

Annual, Reviewed and Academic Journal

Issued By :

Higher Institute of Sciences and Technology, Gharyan

Dr: Melod Mohammed Unis	General Supervision
Dr:Ahmad Ramadan Kobaiz	Editor In Chief
Prof:Abdelati Elalem	Managing Editor
Mr: Mohamed Rajab Baiod	Member
Mr:Mohamed M.Alghiryani	Member
Mr:Abdulbasit Mohamad Ali	Member

Contact Us:

: Telephone   0913506053
E-mail: info@gjt.scitech-gh.edu.ly

Contents

Influence of Operating Conditions on the Performance Parameters of Gas Turbine Cycle Power Plant

Nouralddeen A. Aboud

Higher Institute of Engineering Technology, Gharyan. Libya.

الخلاصة

محور هذه الدراسة يتمركز على إمكانية تشغيل و عمل محطة قدرة التربين الغازي تحت ظروف تشغيل مختلفة، للحصول على ناتج قدرة عالية حسب الظروف المناخية و القيم التصميمية. حيث الموقع الجغرافي و الظروف المناخية تلعب دور كبير في تحسين أداء المحطات الغازية، الكفاءة الحرارية، استهلاك الوقود النوعي، القدرة الإنتاجية. بالإضافة إلى التصميم الهندسي، البنية الداخلية للمادة والتي تدخل تحت دراسة علم المواد. في هذه الورقة تم تقديم دراسة تحليلية على مدى تأثير ظروف التشغيل و درجة حرارة الجو المحيطة على أداء محطة قدرة التربين الغازي. الدراسة تتضمن نموذجا للديناميكا الحرارية للدورة، باعتبار تأثير درجة حرارة الجو المحيط المؤسس على القانون الأول للديناميكا الحرارية. حيث تم الحصول على نتائج باستخدام نموذج رياضي طُور باستعمال برمجة لغة فورتران90 على أساس عرض مقدم في صورة أنماط و مخططات **(graphs and patterns)** توضح تغير مؤثرات الأداء مثل الكفاءة الحرارية و الاستهلاك النوعي للوقود و شغل الضاغط و القدرة الإنتاجية تحت ظروف تشغيل مختلفة كنسبة الانضغاط و درجة حرارة مدخل التربين و درجة الحرارة المحيطة و الكفاءة الأيزنتروبية للضاغط و التربين. حيث يُلاحَظ من النتائج أنه قد تم الحصول على أفضل كفاءة حرارية عند أعلى ظروف تشغيل لنسبة الانضغاط ودرجة حرارة مدخل التربين مع درجة حرارة أقل لمدخل الضاغط ، كذلك يقال بالنسبة لأقل معدل استهلاك النوعي للوقود يمكن الحصول عليه عند تلك الظروف. أما ناتج الشغل النوعي يكون في أفضل الظروف عند نسبة انضغاط 15 عند ظروف تشغيل معينة مع مراعاة الكفاءة الأيزنتروبية للضاغط و التربين، و كما يلاحظ أيضا من النتائج أن درجات الحرارة الأقل عند مدخل التربين، و درجات الحرارة الأعلى عند مدخل الضاغط، لها تأثير على معدل استهلاك الوقود النوعي، هذا وبشكل ملحوظ ذو أهمية كبيرة من حيث اقتصاديات محطات القدرة الغازية.

Abstract

The focus of this study focuses on the possibility of operating and working the gas turbine power plant under different operating conditions, to obtain a high power output according to climatic conditions and design values. Where, the geographical location and climatic conditions play a major role in improving the performance of gas stations, thermal efficiency, specific fuel consumption, and production capacity. As well as the geometrical design, the internal structure of the material which is involved under the study of materials science which came up with special alloys that can withstand high temperatures. In this paper, an analytical study is presented on the effect of operating conditions and ambient air temperature on the cycle performance of a gas turbine plant. The study includes a thermodynamic model for the cycle, considering the effect of ambient temperature based on the first law of thermodynamics. Where results were obtained using a mathematical model developed utilizing the programming language Fortran 90 on the basis of a presentation presented in the form of graphs and patterns showing the variation of performance parameters such as thermal efficiency, specific fuel consumption, compressor work and specific work output under different operating conditions like the compression ratio , turbine inlet temperature(TIT), ambient temperature and isotropic efficiency of the compressor and the turbine. It can be observed from the results that the best thermal efficiency was obtained at the highest operating conditions for the compression ratio and turbine inlet temperature with a lower temperature for the compressor inlet, as well as for the lowest specific fuel consumption rate that can be obtained under the same these conditions. As for the specific work output, it is in the best conditions at a compression ratio of 15 under certain operating conditions, taking into account the isotropic efficiency of the compressor and the turbine. Also, lower temperatures at turbine inlet and higher temperatures at compressor inlet have the influence on the specific consumption rate of fuel. This is significantly of great importance in terms of the economies of power plants.

Index Terms- Gas Turbine; Thermal Efficiency; Ambient Temperature, Compression Ratio, Compressor Inlet Temperature (CIT)
Turbine Inlet Temperature (TIT)

Table (1): List of Symbols, Greek Letters, Subscripts and Abbreviations.

Symbols & Nomenclature			
r_p	Compression ratio (-)	W_{Net}	Net work (Specific work output) ,(kJ/kg)
Cp	Specific heat at constant pressure (kJ/kg.K)	Q_{add}	heat supplied (kJ/kg)
T	Temperature (K), (°C)	P	Pressure (pa)
F	Fuel air mass ratio kg of fuel/kg of air	$\dot{m}$	Mass flow rate (kg/s)
η_c, η_t	The isentropic efficiency for compressor and turbine in the range of (85-90%)		
Greek Letters			
η	Efficiency	r	Specific heat ratio
Subscripts			
1,2,3,4	Points denoted Fig.1and 2	th	Thermal efficiency
A	Air	f	Fuel
T	Turbine	g	Flue gas
C	Compressor		
Abbreviations			
W	Work	HR	Heat rate (kJ/kWh)
GT	Gas turbine	LHV	Lower heating value (kJ/kg)
TIT	Turbine inlet temperature (k)	SFC	Specific fuel consumption (kg/kW.h)
CIT	Compressor inlet temperature (k)		

1. INTRODUCTION

Gas turbines play a vital role in industry and electrical power generation. They are important part in the field of mechanical drive, gas transmission and power generation. Where, become very popular as a result of the high power to weight ratio, compactness, and ease of installation. Performance of the gas turbines cycle power plant mainly depend on the cycle compression ratio, turbine inlet temperature and ambient air conditions. As well as the material science which came up with special alloys that can withstand high temperatures, enabled the gas turbine to enter a new competition as a main power plant for generating electricity.

The low efficiencies of the gas turbine plants are tired to many factors which include: operation mode, poor maintenance procedures, age of plant, discrepancies in operating data, high ambient temperature and relative humidity. Power output and efficiency of a gas turbine plant depends largely on the condition of the compressor inlet air temperature (Cortes and William, 2003) [1].

M. M. Rahman et al [2] evaluated in their study of the thermodynamic performance analysis of gas-turbine power-plant, They concluded that the compression ratio, ambient temperature, air to fuel ratio as well as the isentropic efficiencies are strongly influence on the thermal efficiency. In addition, the thermal efficiency and power output decreases linearly with increase of the ambient temperature and air to fuel ratio. Also, the specific fuel consumption and heat rate increases linearly with increase of both ambient temperature and air to fuel ratio. Moreover, thermodynamic parameters on cycle performance are economically feasible and beneficial for the gas turbine operations.

Anoop and Onkar [3] investigated the effect of compressor inlet temperature & relative humidity on gas turbine cycle performance. Investigation reported that there was 0.77 percent increase in the specific power output and 0.65 percent increase in thermal efficiency for every 15 percent increase of relative humidity of GT cycle power plants. Also there was 10.12 percent gain in the specific work output, 3.45 percent in thermal efficiency and 3.43 percent saving of fuel by decreasing the compressor inlet temperature from 318K to 282K.

Thamir K. Ibrahim1 et al [4] studied the influence of operation conditions and ambient temperature on performance of gas turbine power plant. They concluded that the peak efficiency, power and specific fuel consumption

occur when compression ratio increased. Maximum power for the turbine inlet temperatures are selected a compression ratio 6.4 for a turbine inlet temperature of 1000K result in a higher thermal efficiency.

2. MODELING OF GAS TURBINE CYCLE (The Brayton Cycle)

A simple gas turbine consists of four main sections a compressor, a combustor, a power turbine and generator. As shown in figure (1). The compressor supplies a fresh air at high pressure to combustion chamber, which provides a power turbine and flue gas at high temperature and pressure.
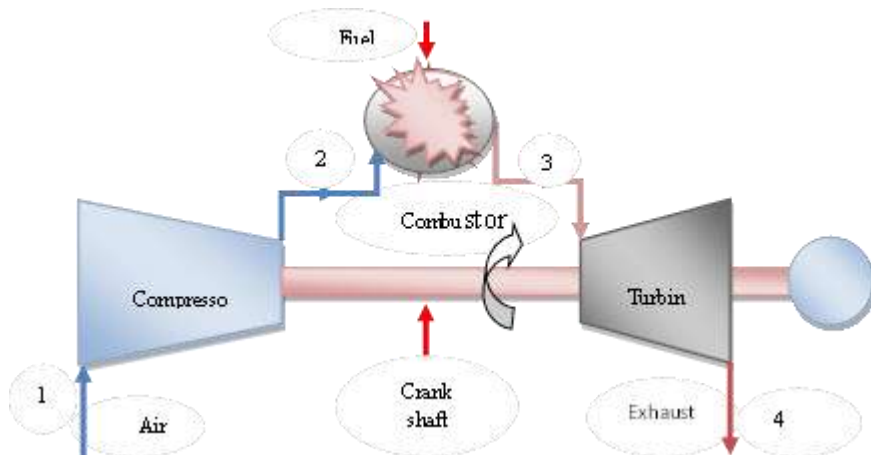
Figure (1): schematic diagram for a simple gas turbine

A combustor converts the thermal energy from a combustible fuel to the mechanical energy, where the air is mixed with fuel, and burned under constant pressure conditions in the combustor. The turbine module is important part of gas turbine cycle that it extracts power from hot burnt gases flow, resulting by the combustion of fuel with air. The electrical generator is connected directly with turbine module to convert the kinetic (mechanical) energy into electrical energy produces nearly all of the electricity that consumers use. The compressor module, combustor module, turbine module, connected by one or more shafts are collectively called gas generator.

The Gas Turbine Cycle:

The Brayton cycle is the cycle which the engineers and researchers make it the reference for them to compare and try to reach. In reality, the gas turbine does not work as the ideal Brayton cycle. It works under many effects, such that both the compression process (1-2) with fluid friction and the expansion process (3-4) with fluid friction results in an increase in entropy. The ideal processes and actual processes are represented in full line and dashed line, respectively, on the T-S diagram as shown in Figure (2).These parameters in terms of temperature are defined as [15]:

(a)   **(b)**
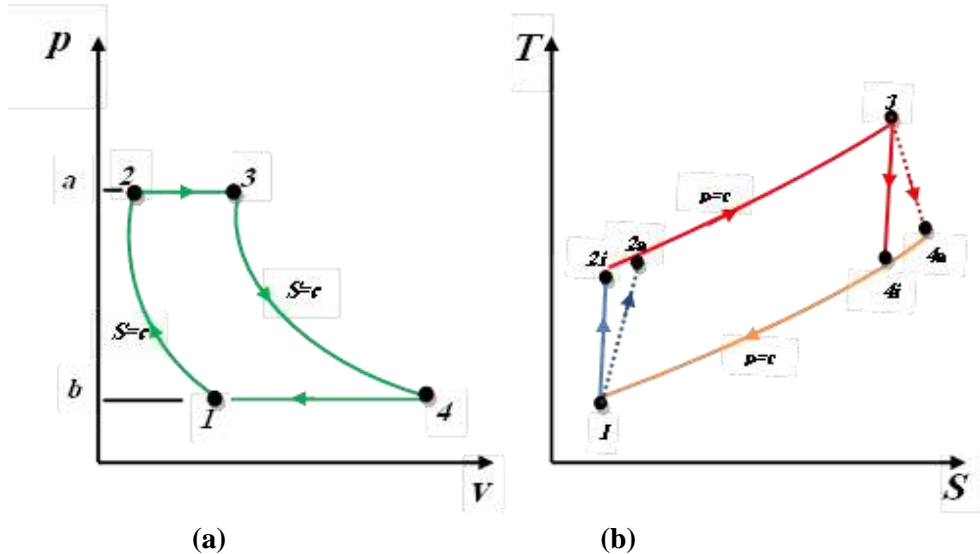
Figure (2): (a) P-V diagram and (b) T-S diagram of ideal and non-ideal Brayton cycle (a indicates actual process)

The compression ratio for the compressor (*rp*) can be defined as eq. (1):

$$r_p = \frac{P_2}{P_1} \qquad (1)$$

The isentropic efficiency for compressor and turbine in the range of as eq. (2):

$$\eta_c = \frac{T_{2s}-T_1}{T_2-T_1} \qquad \text{And} \qquad \eta_t = \frac{T_3-T_4}{T_3-T_{4s}} \qquad (2)$$

The final temperature of the compressor is calculated in eq. (3)

$$T_2 = T_1 + \frac{T_{2s} - T_1}{\eta_c} = T_1 \left(1 + \frac{r_p^{\frac{\gamma_a - 1}{\gamma_a}} - 1}{\eta_c} \right) \tag{3}$$

So, the work of the compressor (W_c) when blade cooling is not taken into account can be calculated in eq. (4)

$$W_c = \left(\frac{c_{pa'avg} \, T_1 \left(r_p^{\frac{\gamma_a - 1}{\gamma_a}} - 1 \right)}{\eta_m} \right) \tag{4}$$

Where $C_{pa'avg}$ is the specific heat of the dry air at constant pressure, determined as a function of the average temperature across the compressor (Alhazmy, M.M and Najjar,Y.S.H.,2004) [10]. It can be fitted by eq. (5) for the range of 200 K < T < 800 K [11]:

$$C_{Pa}(T) = 1.04841 - \left(\frac{3.8371T}{10^4} \right) + \left(\frac{9.4537T^2}{10^7} \right) - \left(\frac{5.49031T^3}{10^{10}} \right) + \left(\frac{7.9298T^4}{10^{14}} \right) \tag{5}$$

Where, CIT $_= T_a$ in Kelvin.

The specific heat of flue gas is given by eq. (6) [12]:

$$C_{Pg}(T) = 0.991615 + \left(\frac{6.99703T}{10^5} \right) + \left(\frac{2.7129T^2}{10^7} \right) - \left(\frac{1.22442T^3}{10^{10}} \right) \tag{6}$$

From energy balance in the combustion chamber

$$\dot{m}_a c_{pa} T_2 + \dot{m}_f \times LHV + \dot{m}_f c_{pf} T_f = (\dot{m}_a + \dot{m}_f) c_{pf} \times TIT \tag{7}$$

Where, T_3 = TIT, is turbine inlet temperature.

After manipulating from (7), the ratio of mass flow rate (*f*) is expressed as eq. (8):

$$f = \frac{\dot{m}_f}{\dot{m}_a} = \frac{c_{pg} \times TIT - c_{pa} T_2}{LHV - c_{pg} \times TIT} \tag{8}$$

Where *LHV* is the lower heating value of the fuel (natural gas; 48235.63 KJ/kg) [13], ($\dot{m}_f$) is the mass flow rate of fuel, and ($\dot{m}_a$) is the mass flow rate of air.

The shaft work (W_t) of the turbine is given by eq. (9):

$$W_t = c_{pg'avg} \times TIT \times \eta_t \left(1 - \frac{1}{r_p^{\frac{\gamma_g-1}{\gamma_g}}} \right) \qquad (9)$$

Where $C_{pg'avg}$ is the flue gas specific heat at constant pressure, calculated as a function of the average temperature across the turbine (Alhazmy, M.M and Najjar,Y.S.H.,2004) [10].

The network of the gas turbine (W_{net}) is calculated from the equation (10):

$$W_{net} = c_{pg'avg} \times TIT \times \eta_t \left(1 - \frac{1}{r_p^{\frac{\gamma_g-1}{\gamma_g}}} \right) - c_{pa}T_1 \left(\frac{r_p^{\frac{\gamma_a-1}{\gamma_a}}}{\eta_c} \right) \qquad (10)$$

Also, the output power from the turbine (P) can be expressed as eq. (11):

$$P = \dot{m}_a \times W_{net} \qquad (11)$$

The heat supplied (Q_{add}) is formulated as eq. (12):

$$Q_{add} = c_{pg'avg} \times \left[TIT - T_1 \times \left(1 + \frac{r_p^{\frac{\gamma_a-1}{\gamma_a}}-1}{\eta_c} \right) \right] \qquad (12)$$

Where $C_{pg'avg}$ is the flue gas specific heat at constant pressure, calculated as a function of the average temperature across the combustion chamber (Alhazmy, M.M and Najjar,Y.S.H.,2004) [10].

The performance parameters of the gas turbine cycle power plant are specific work output (network), specific fuel consumption, cycle efficiency and heat rate and are calculated from the following governing equations.

$$W_{net} = W_t - W_c \qquad (13)$$

$$SFC = \frac{3600f}{W_{net}} \qquad (14)$$

$$\eta_{th} = \left(\frac{W_{net}}{Q_{add}} \right) \qquad (15)$$

The heat rate (HR) which is the consumed heat to generate unit energy of electricity can be expressed as eq. (16).

$$HR = \frac{3600}{\eta_{th}} \qquad (16)$$

3. RESULTS AND DISCUSSION

This paper presents the simulation results of effect of ambient temperature and operating conditions on the performance of the gas turbine cycle as the power output and thermal efficiency. The operating parameters like ambient temperature, turbine inlet temperature Compression ratio are calculated using Fortran90 for carrying out the analysis.

Figure (3) depicts the relation between the ambient temperature and the thermal efficiency for several different values of turbine inlet temperature. It can be observed that the increase in ambient temperature leads to an increase in the specific work of compressor that is decreased of specific work output of gas turbine cycle. Thus reduce cycle efficiency for gas turbine, so when the turbine inlet temperature is risen, this leads to an increase in the thermal efficiency. It can be said that the thermal efficiency linearly increases with rises of turbine inlet temperature, while decreases with increases of ambient temperature.
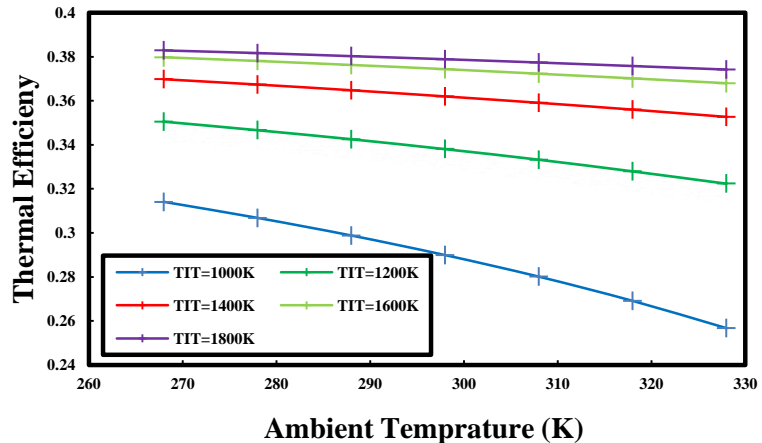

Figure (3): Effect of ambient temperature and turbine inlet temperature on thermal efficiency.

The effect of ambient temperature and turbine inlet temperature on specific fuel consumption is shown in Figure (4), where can be watched that specific fuel consumption increases linearly with increases of ambient temperature and lower turbine inlet temperature. Also, on the other hand the

specific fuel consumption decreases with increases of turbine inlet temperature; we notice a sudden increase in the rate of fuel consumption at lower turbine inlet temperature with increases ambient temperature, which means that the combustion of fuel is incomplete, therefore should be increased turbine inlet temperature with take into consideration the burning of fuel.

In figure (5) represents the variation of thermal efficiency with different gas turbine cycle compression ratio on various compressor inlet temperatures (CIT). Here the thermal efficiency decreases with increase in compressor inlet temperature for varying compression ratios. However, the increase in compression ratio gives increment in power output as a result of thermal efficiency increase. Also we can note that the effect of ambient temperature on the thermal efficiency of cycle is relatively low, when compared with the effect of different compression ratios.
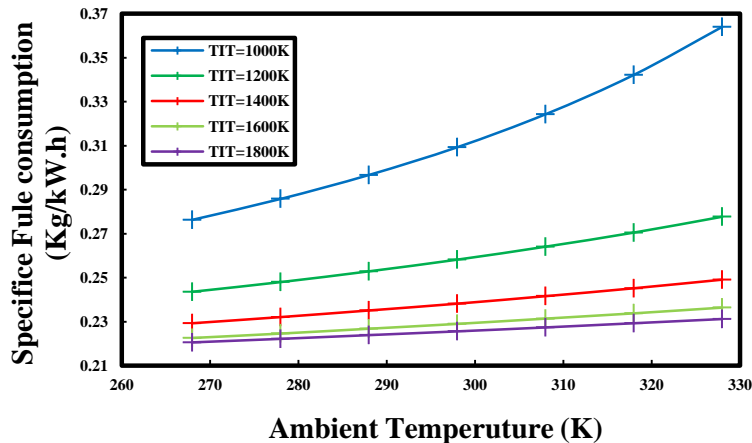

Figure (4): Variation of specific fuel consumption of GT power cycle with different ambient temperature and turbine inlet temperature.
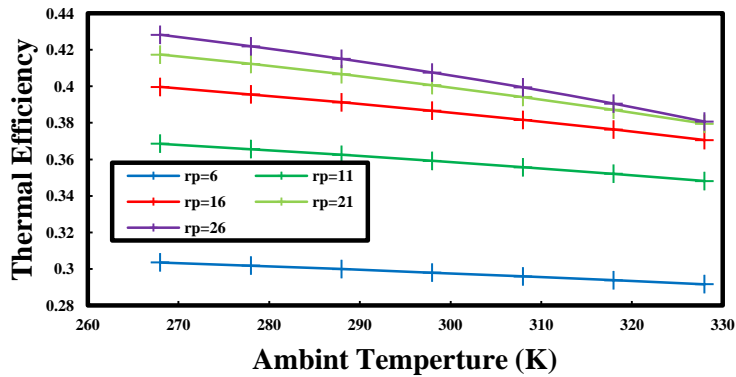
Figure (5): Variation of thermal efficiency against the ambient temperature and compression ratio.

Figure (6) shows the variation between thermal efficiency and compression ratio for several different values of turbine inlet temperature, where the thermal efficiency almost linearly increases at lower compression ratio, especially, when the turbine inlet temperature is increased. The thermal efficiency turns at certain value of compression ratios, this means that the thermal efficiency depends on the turbine inlet temperature. There is a sharp drop in the thermal efficiency at lower turbine inlet temperature, which indicates the need to increase the fuel quantity and the turbine inlet temperature to improve the efficiency of the cycle.
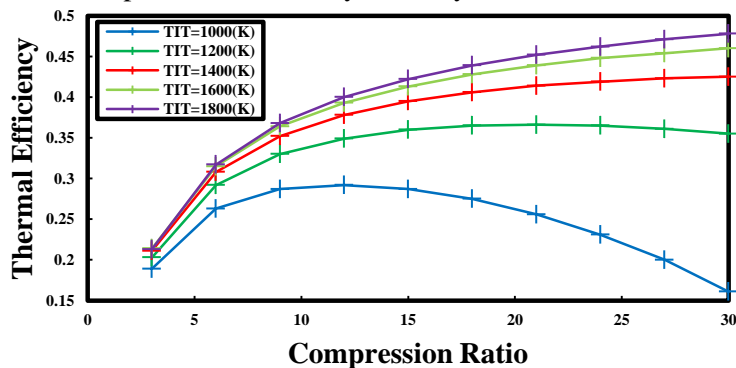
Figure (6): Variation of thermal efficiency on compression ratio and turbine inlet temperature.

Figure (7) presents the relation between specific fuel consumption (SFC) against the compression ratio and turbine inlet temperature. Here it is observed that the (SFC) decreases with increases of compression ratio and turbine inlet temperature at certain value, after that gradually increases

dramatically for lower turbine inlet temperature (TIT). It is also noted that the turbine inlet temperature should be increased at a certain value only then it is stopped, because the rate of specific fuel consumption becomes almost constant at higher turbine inlet temperatures. In figure (8) shows the variation of compressor work with different compression ratio on various ambient temperatures. Here the compressor work increases with the increase of compression ratio and the ambient temperature. Also we can say that the isentropic compressor efficiency plays a major role in increasing the thermal efficiency of gas turbine cycle.
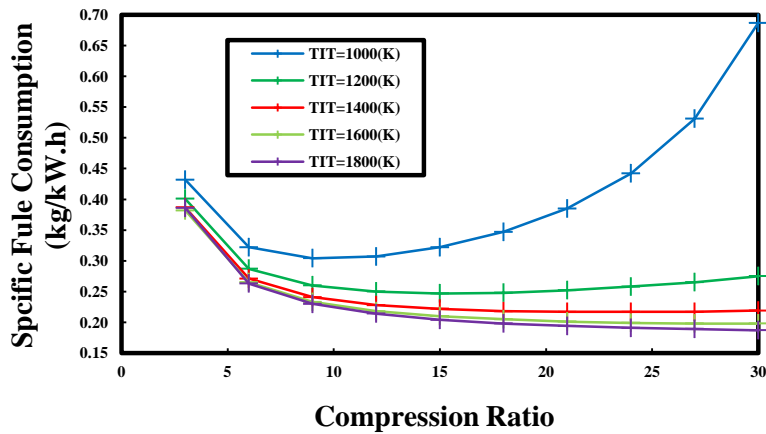
Figure (7): Variation of specific fuel consumption of GT power cycle with different compression ratio and turbine inlet temperature.
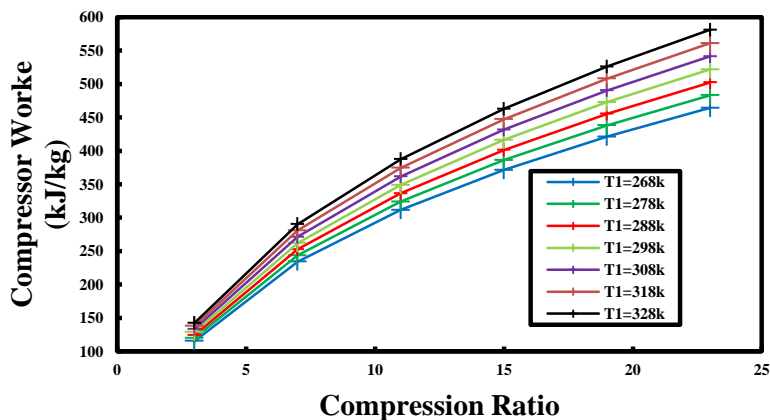

Figure (8): Variation of compressor work of GT power cycle with different compression ratio and ambient temperature.

Figure (9) illustrates the effect of compression ratio and ambient temperature on the specific work output. It can be evident that specific work output initially increases at higher value for compression ratio by 7 to 15, after that the increase in specific work becomes slower, because of increasing component of compression work.
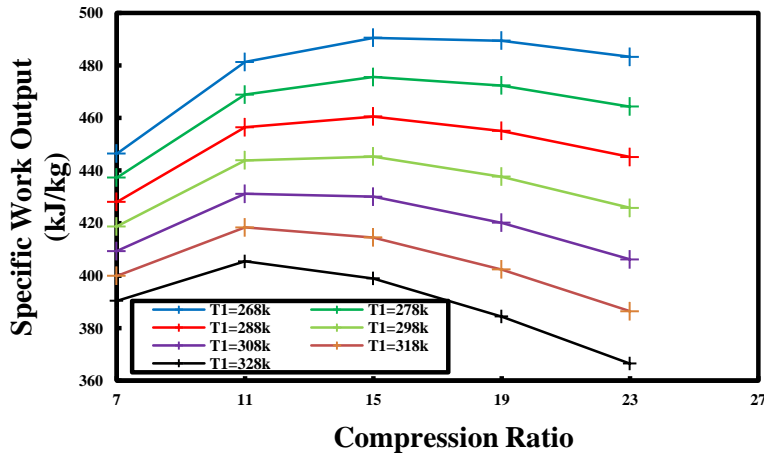
Figure (9): Variation of specific work output of GT power cycle with different compression ratio and ambient temperature.

Figure (10) describes the effect of compression ratio and compressor inlet temperature (CIT) on specific fuel consumption. It can be noticed a reduction in the specific fuel consumption rate with increase of compression ratio. Also, the specific fuel consumption increases with increasing compressor inlet temperature (CIT). However, an increase and decrease of compression ratio and ambient temperature of gas turbine cycle determine the extent of fuel economy and consumption.

The effect of compression ratio on the thermal efficiency of the gas turbine cycle on various compressor inlet temperatures (CIT) is shown in Figure (11). It can be seen that the thermal efficiency values are very close at lowest compression ratio 3 on different ambient temperature. This indicate that the effect of ambient temperatures are relatively little, increasing the compression ratio of the gas turbine cycle produces more specific work output at lower compressor inlet temperature which give more thermal efficiency
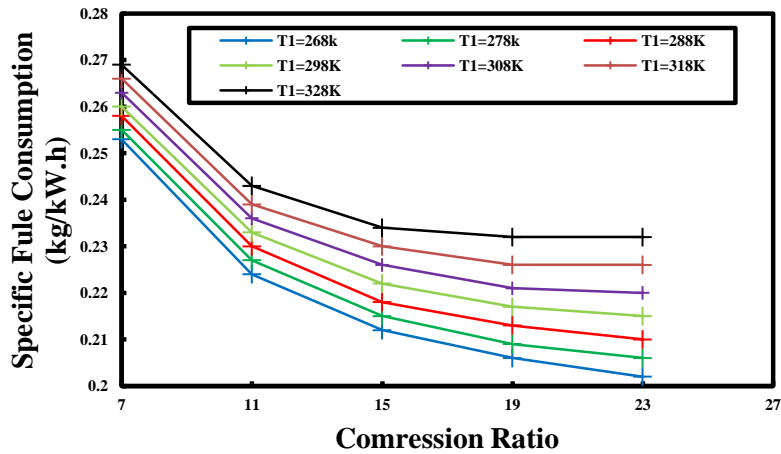
Figure (10): Variation of specific fuel consumption of GT power cycle with different cycle pressure ratio and ambient temperature.
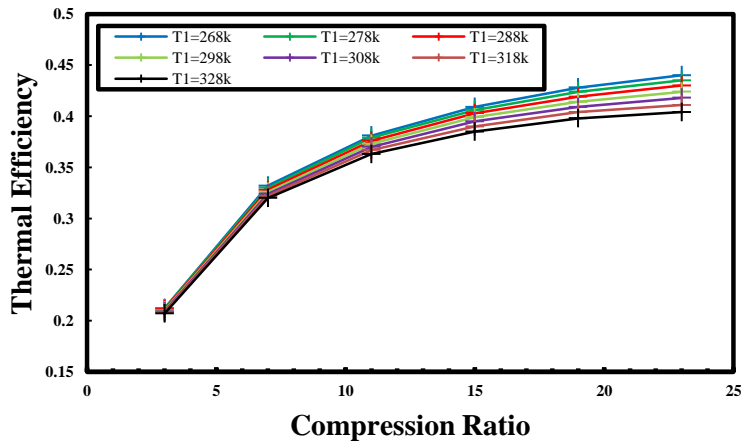
**Figure (11): Variation of thermal efficiency with compression ratio and ambient temperature.**

5. CONCLUSIONS

In this the present study the simulation results has been obtained by a developed computational model using Fortran90, which gives the influence of operating conditions on the gas turbine power plant. The results of this study were summarized below:

1- In general, the operating parameters like ambient temperature, compression ratio, turbine inlet temperature have significantly the influence on the performance parameters of gas turbine cycle.

2- Increasing the compressor inlet temperature increases the specific fuel consumption rate and decreases the thermal efficiency of cycle.

3- Increasing in the compression ratio increases the specific work output which increases the thermal efficiency. Also, decreases the specific fuel consumption rate.

4- The compressor work increases with increasing the compression ratio and compressor inlet temperature that decreases the specific work output as result for decrease the thermal efficiency.

5- Maximum efficiency and minimum specific fuel consumption rate are at higher compression ratio and turbine inlet temperature with lower ambient temperature.

References

[1] Cortes, C.R. and D.F. Williams, 2003. Gas turbine inlet air cooling techniques: An overview of current technologies. Power-Gen International, Las VegasNeva, USA.

[2] M. M. Rahman1, Thamir K. Ibrahim1 and Ahmed N. Abdalla,2011, International Journal of the Physical Sciences Vol. 6(14), pp. 3539-3550.

[3] Anoop Kumar Shukla & Onkar Singh ,May-2014, Effect of compressor inlet temperature & relative humidity on gas turbine cycle performance, international journal of scientific & engineering research, volume 5, issue 5,pp.664-671.

[4] Thamir, K. Ibrahim, Rahman, M.M., and Ahmed, .N. Ab-dAlla, 2010, Study on the effective parameter of gas turbine model with intercooled compression process, Scientific Re-search and Essays, Vol. 5, No. 23, pp. 3760-3770.

[5] Rahman, M.M., Thamir, K. Ibrahim, Kadirgama,K., Mamat R. and Bakar, R.A., 2011, Influence of operation conditions and ambient temperature on performance of gas turbine power plant, Adv. Mater. Res., Vol. 189-193, pp. 3007-3013.

[6] Thamir, K. Ibrahim, Rahman, M.M. and Ahmed, N. AbdAlla, 2010, Improvement of gas turbine performance based on in-let air cooling systems: A technical review, International Journal of Physical Sciences, Vol. 6, No. 4, pp. 620-627.

[7] Rahman, M.M., Thamir, K. Ibrahim, Taib, M.Y., Noor, M.M., Kadirgama, K., and Bakar, R.A., 2010, Thermal analysis of open-cycle regenerator gas-turbine power-plant, International Journal of Mechanical and Mechatronics Engineering, Vol:4, No:8, pp. 701-706.

[8] Thamir K. Ibrahim1, M. M. Rahman, 2012, Effect of compression ratio on performance of combined cycle gas turbine, vol. 2, no. 1, pp. 9-14.

[9] Thamir K. Ibrahim and M.M. Rahman, December 2010,Effects of operation conditions on performance of a gas turbine power plant, national conference in mechanical engineering research and postgraduate studies (2nd NCMER 2010), UMP Pekan, Kuantan, Pahang, Malaysia; pp. 135-144.

[10] Alhazmy, M.M and Najjar,Y.S.H.,2004,''Augmentation of gas turbine performance using air coolers'', Applied Thermal Engineering Vol.24,N.2-3,pp.415-429.

[11] R. Hosseini, A. Beshkani, M. Soltani, Performance improvement of gas turbines of Fars (Iran) combined cycle power plant by intake air cooling using a media evaporative cooler, Energy Conversion and Management 48, 1055–1064, 2007.

[12] S. O. Oyedepo and O. Kilanko, 2014 , Thermodynamic Analysis of a Gas Turbine Power Plant Modeled with an Evaporative Cooler, International Journal of Thermodynamics (IJoT) Vol. 17. No. 1, pp. 14-20.

[13] Ana Paula Santos, Cláudia R. Andrade,2012, Analysis of Gas Turbine Performance with Inlet Air Cooling Techniques Applied to Brazilian Sites, J. Aerosp. Technol. Manag., São José dos Campos, Vol.4, No 3, pp. 341-353.

[14] K.Y.AL-Salman, Q.A. Rishack and S.J. AL-Mousawi,2007, Parametric Study Of Gas Turbine Cycle With Fogging System, J.Basrah Researches (Sciences) Vol. 33. No.4, pp.16 -30.

[15] A.F. Al-Sayed: Aircraft Propulsion and Gas Turbine Engines (Taylor & Francis, USA, 2008), ISBN 978-0-8493-9196-5.

Tamper Detection in Multimodal Biometric Authentication Systems Using Fragile Fingerprint Watermarking and Convolutional Neural Networks

Abdulmawla Najih*[, 1], Nooreddin Hemidat[2,] Abier Belashher[3]

[1*2]Department of computer engineering, The Higher Institute of Science & Technology Gharian, [3]Department of computer engineering, Faculty of Engineering,University of Tripoli

[*]nabdulmawla@gmail.com

الملخص

النمو السريع في توظيف المصادقة البيومترية متعدد الوسائط لحماية المعلومات والخدمات لاقت اهتمامًا كبيرًا لاستخدامها في تأمين نقاط الضعف في هذه الأنظمة. تعد العلامة المائية الرقمية إحدى التقنيات الرئيسية المستخدمة لضمان أمان هذه الأنظمة. يسمح استخدام العلامة المائية الرقمية للمصادقة البيومترية بالتعرف على الصور الاصلية التي يتم ارسالها بين الأجزاء المختلفة من النظام، أو المخزنة في قاعدة البيانات. ويمكن أيضًا استخدام العلامات المائية الهشة للكشف عن اختراق والتلاعب في الصور، بالإضافة إلى مهمة التعرف على الصور الاصلية. في هذه الدراسة، تم اقتراح تقنية العلامة المائية الرقمية الهشة، والتي تستخدم صورة بصمة الإصبع كعلامة مائية على صور الوجه. تجمع الطريقة المقترحة بين تقنية تحويل جيب التمام المنفصل (DCT) وتقنية العلامة المائية للبت الأقل أهمية (LSB) يسمح هذا المزيج بضغط الصورة ذات العلامة المائية، حيث إنه يعالج نسخة DCT لصورة الغلاف، مع الحفاظ على هشاشة العلامة المائية، باستخدام تقنية LSB. علاوة على ذلك، تقوم الطريقة أيضًا بتشفير صورة بصمة الإصبع، باستخدام Arnold Transformation، لإضافة طبقة أخرى من الأمان إلى نظام المصادقة البيومترية. وقد اظهرت نتائج التقييم أن الطريقة المقترحة قد تفوقت على أحدث الأساليب الموجودة في الدراسات السابقة، لأنها تحافظ بشكل كبير على المعلومات في كل من بصمة الإصبع والصور الحيوية الأخرى، بحيث يمكن استخدام كليهما في المصادقة العملية دون الحاجة إلى استخدامها بشكل منفصل.

الكلمات المفتاحية: المصادقة متعددة الوسائط البيومترية، علامة مائية هشة، تحويل جيب التمام منفصلة، البت الأقل أهمية، بصمات الأصابع.

Abstract

The rapid growth of multimodal biometric authentication employment to protect information and services has attracted significant attention toward securing the vulnerabilities in these systems. One of the main techniques that are used to improve the security of these systems is digital watermarking. The use of digital watermarking allows the biometric authentication to recognize the authenticity of the images communicated among the different parts of the system, or stored in a database. Fragile watermarking can also be employed for tamper detection, in addition to the authenticity recognition task. In this study, a fragile digital watermarking technique is proposed, which uses the fingerprint image as a watermark on face images. The proposed method combines the Discrete Cosine Transform (DCT) and Least Significant Bit (LSB) watermarking technique. This combination allows the compression of the watermarked image, as it manipulates the DCT version of the cover image, while maintaining the fragility of the watermarking, using the LSB technique. Moreover, the method also encrypts the fingerprint image, using Arnold Transformation, to add another layer of security to the biometric authentication system. The evaluation results show that the proposed method has outperformed the state-of-the-art methods existing in the literature, as it highly maintains the information in both the fingerprint and the other biometric images, so that, both can be used in the authentication process without the need to communicate them separately.

Keywords: Multimodal biometric authentication; fragile watermarking; Discrete Cosine Transform; Least Significant Bit; Fingerprints.

I. INTRODUCTION

Biometric authentication systems are being widely employed to protect information and services from any unauthorized access. These systems have shown better resistance to simple attacks, such as shoulder surfing, which the earlier secret-based systems suffer from [1, 2]. However, the use of biometric authentication still suffers from vulnerabilities at different positions of the system. One of the main concerns in these systems is the authenticity of the images received from the sensors or stored in the models' database [3]. Image

processing tools can be used to manipulate these images and change certain features in order to gain unauthorized access to the system [4]. To verify the authenticity of the received images, two main approaches are used, which are the cryptography based [5, 6] and fragile watermarking based approaches [7, 8]. In cryptography based approaches, a hash function is used to calculate a message authentication code, which is compared to the code calculated for the received image, using the same hash function, in order to verify the authenticity of the received image. In fragile watermarking based approaches, a watermark is inserted in the image before being transmitted, where the receiver verifies the authenticity of the image by investigating the existence of the watermark. However, the existing watermarking techniques insert static watermarks, or watermarks related to features from the image being protected, so that, the receiver can extract this information from the image and validate the watermark to detect any tampering [9].

With the growing importance and sensitivity of information and services protected by biometric authentication systems, and according to the better accuracy and wider population coverage of multibiometric authentication systems, these systems are being widely used in the recent years [10]. Such systems extract biometric features from multiple body parts of the user authenticating into the system. Many of these systems rely on extracting features from the fingerprint and face images, according to the high availability, distinctiveness and robustness of these biometrics [11, 12] and the ability of collecting the face image, passively, during the collection of the fingerprint [13]. However, in addition to the importance of the authenticity verification of the stored model images and those collected from the user, it is important to maintain the biometric features in these images as intact as possible, to maintain the accuracy of the authentication system [14]. Moreover, watermarking techniques are used to embed one of the images in the other, in order to reduce the bandwidth required by the authentication system to communicate these images [15].

A hybrid digital watermarking technique is proposed by Vatsa et al. [16] that watermarks the face image information on the fingerprint image, by combining the Discrete Wavelet Transform (DWT) and LSB techniques. To increase the efficiency of the watermark data, the two-dimensional Gabor of the face image is calculated and used as the watermark data on fingerprint images. The results of this study show that the watermarking technique has been able to survive through different geometric and frequency attacks. Thus,

the proposed bimodal authentication system has been able to significantly maintain the recognition rate, despite the application of multiple attacks. However, the use of such approach does not allow the detection of any tampering, where some information in the cover photo may be manipulated to produce a false authentication.

Thanki and Borisagar [17] propose a fragile watermarking technique that hides the fingerprint image, as the watermark, in the face image, as the cover image. This method combines the Singular Value Decomposition (SVD) to embed the details wavelet of the DWT of the fingerprint image, which is encrypted using the Compressive Sensing (CS) technique, to add another layer of protection. Although the watermark data are compressed, to reduce the distortion imposed on the cover image, no compression is applied to the cover image, which increases the storage required to store these images and the bandwidth required to communicate them. However, the fragility of this technique has enabled the detection of any tampering with the watermarked image, as the similarity measures between the original watermark and the received one is very low when the watermarked image is attacked. Similarity, the method proposed in [18] also uses the CS theory but combined with the Fast Discrete Wavelet Transform. Despite the lower effect of this method, imposed by the watermark over the cover image, the results show that compressing the image results in losing the watermark information. Hence, the watermarked images are required to be stored and communicated in full size. Such requirement increases the resources consumption of the system, i.e. the storage space and bandwidth. Moreover, the fragile watermarking technique proposed in [19] also uses Discrete Wavelet Transform (DCT) but does not consider compressing the watermarked image.

A watermarked image can be compressed when a robust watermarking technique is used. Nafea et al. [20] present a hybrid watermarking technique that uses the Discrete Wavelet Transform-Singular Value Decomposition. The results of the evaluation experiments show that the watermarked image survives compression, up to a certain rate. However, as a robust watermarking technique, tamper cannot be detected in an images watermarked using such technique [21, 22]. Hence, despite the reduction in the resources consumption when such a method is used, tampering cannot be detected, especially when an attack targets certain region of the image.

To reduce the effect of the watermark information on the cover image and reduce the size of the watermarked image, by allowing the use of smaller

cover images, the method proposed by Ma et al. [23] down samples the watermark image. The face images are used as the watermark, for the fingerprint image, and are reduced to only 8×8 pixels before being used as the watermark. Accordingly, the facial features cannot have significant influence in the authentication stage, as these features are downsized, according to the results of the conducted experiments. However, the results show that the method has been able to protect the watermarked images, as the watermark information is lost when any attack is applied to the watermarked image.

This paper proposes a hybrid fragile watermarking technique that combines Discrete Cosine Transform (DCT) and Least Significant Bit (LSB) techniques. The use of the DCT format of the image allows compressing it before being stored or communicated, which reduces the storage and bandwidth required by the authentication system, while the use of the LSB method provides the required fragility to detect any tampering in the image. JPEG image format, which is the most widely used compressed image format [24, 25], relies of DCT to eliminate cosine frequencies that have least magnitude in the image. However, the use of LSB watermarking technique prior to applying the DCT eliminates the entire watermark information during compression. Thus, the proposed method applies the LSB algorithm to the DCT values of the image, instead of the actual pixels' values. The use of the fingerprint image as a watermark in the face image reduces the size of the stored and communicated data. However, the proposed method maintains two important conditions, which are preserving the information in both images as intact as possible, and detect any tampering occurs to the resulting watermarked image. As the watermark information in the proposed method is not extracted from the cover image, tamper detection at the receiving end cannot be achieved using the traditional techniques. Thus, a Convolutional Neural Network (CNN) is trained to recognize the patterns in fingerprint images, so that, is such patterns are not detected, the image is considered unauthentic.

The remainder of this paper is organized as follows. Section II describes the proposed techniques to implement the tamper detection method, which are the watermarking and fingerprint patterns detection techniques. Section III describes the dataset used for the evaluation process and the adjustments conducted to produce more appropriate sets. Section IV describes the experimental setup and the performance measures of the proposed methods.

Section V presents the conclusions of this study and the future work that may improve the performance of the proposed methods.

II. PROPOSED METHOD

JPEG image compression standard [26] uses two compression stages to reduce the size of a still image. The first stage uses lossy compression based on calculating coefficient values of cosine waves with 64 different frequencies for each 8×8 pixels in that image. Then, the resulting values are divided by corresponding values in a predefined quantization table, which mainly reduces the effect of higher frequencies as they normally have less visual effect on the image. The resulting values are then rounded to the nearest integer, in order to reduce the number of unique values in the resulting matrix. Up to this level of JPEG compression, the size of the resulting matrix is identical to the size of the original image, as each 8×8 pixels are replaced with 8×8 values that represent the quantized cosine coefficients. The second stage executes lossless compression using Huffman encoding, which makes use of the lower number of unique values, to reduce the size of the resulting matrix before communicating or storing the image. The proposed method interacts with the quantized values, before being compressed using Huffman encoding, or being used to retrieve the original pixels values of the image.

A. DIGITAL WATERMARK EMBEDDING

The proposed method uses the fingerprint image as the watermark to be inserted to the face image. Fingerprints impressions generated by the ripples on the surface of the finger skin, where each pixel in the image can be either belong to a ripple or not. Thus, binarizing the fingerprint image does not cause loss in the biometric information that can be extracted from it [27]. However, binarization the image can significantly reduce the size of the data required to describe the fingerprint, which reduces the distortion it imposes over the cover image, which is the face image. Before binarizing the fingerprint image, the image is resized to fit into the face image, if the fingerprint image is larger than the face image, using linear interpolation method [28]. Then, the intensity histogram of the image is equalized, to improve the quality of the binarized image.

To improve the security of the proposed watermarking method, the binarized fingerprint image is scrambled using Arnold Transform. This scrambling technique requires a secret key that consists of three number. The

first two number are any pre-shared secret numbers that are used in Equation 1 to calculate the new position of a point located at (*x*, *y*) coordinates based on its previous coordinates, while the third number represents the number of iterations that the encoding is applied over the image [29, 30]. Thus, these numbers can be set to static values or time-sensitive values to deny any replay attacks

$$\begin{bmatrix} x_i \\ y_i \end{bmatrix} = \begin{bmatrix} 1 & a \\ b & ab+1 \end{bmatrix} \begin{bmatrix} x_{i-1} \\ y_{i-1} \end{bmatrix} mod(D) \tag{1}$$

The scrambled version of the binarized fingerprint image is then used to manipulate the LSB of the DCT coefficient values, calculated from the face image. As the dimensions of the fingerprint image is equal to or less than the dimensions of the face image, and as each pixel value in the fingerprint image can only be zero or one, it is guaranteed that LSBs of the face image can handle the entire information of the fingerprint image. Finally, Huffman encoding is applied to the manipulated values before storing or communicating the resulting values in JPEG format, as shown in Algorithm 1.

Algorithm 1: Watermark Embedding

Input: Fingerprint image, Face image, Arnold keys
(a, b,   i)
1: FL, FW ← Length and width of face image
2: PL, PW ← Length and width of fingerprint image
3: if PL>FL:
   Fingerprint ← Resize(Fingerprint, FL/PL)
   PL, PW ← Length and width of fingerprint image
3: if PW>FW:
   Fingerprint ← Resize(Fingerprint, FW/PW)
   PL, PW ← Length and width of fingerprint image
4: Fingerprint ← EqualizeHist(Fingerprint, (0,255))
5: for x = 0 to PW:
     for y = 0 to PL:
        if Fingerprint[x,y] > 127:
           Fingerprint[x,y] ← 1
        Else:
           Fingerprint[x,y] ← 0

6: Fingerprint ← Arnold Transform(Fingerprint, (a,
b, i))
7: FDCT ← DCT(Face)
8: FDCT ← Quantize(FDCT)
9: for x = 0 to PW:
   for y = 0 to PL:
     FDCT[x,y].LSB ← Fingerprint[x,y]
10: FDCT ← Huffman_Encode(FDCT)
Output: FDCT

B. Fingerprint and Face Images Extraction

When the compressed watermarked image is received, the fingerprint and face images are extracted. Both images are used for biometric authentication, while the fingerprint image is also used to detect any tampering with the watermark image. The first step to retrieve these images is to decompress the Huffman-encoded values. As the dimensions of the fingerprint image are constant, depending on the specification of the sensor used to collect these images, these dimensions are known to the receiver of the watermarked image. These dimensions are compared to the dimensions of the received image in order to recognize the area that contains the data of the fingerprint image. By collecting the LSBs of the received coefficient values, the original values of the scrambles binarized fingerprint image can be retrieved. Then, using the same keys used to scramble the fingerprint data, inverse Arnold transformation is used to reconstruct the original binarized fingerprint image. Finally, by applying inverse DCT to the received coefficients, the face image can also be reconstructed. Algorithm 2 describes the main steps required to retrieve the fingerprint and face images from the received compressed coefficient values.

Algorithm 1: Fingerprint and face image extraction

Input: Compressed DCT coefficients, Fingerprint
length   (PL) and width (PW), Arnold keys (a,
b, i)
1: Coeff ← Huffman_Decode(Compressed)
2: FL, FW ← Length and width of Coeff
3: if PL>FL:
  PW ← int(FL/PL)
  PL ← FL

4: if PW>FW:

  PL ← int(FW/PW)

  PW ← FW

5: Fingerprint ← Empty_array(PW, PL)

6: for x = 0 to PW:

    for y = 0 to PL:

       Fingerprint[x,y] ← Coeff[x,y].LSB

7: Fingerprint ← Inverse Arnold

Transform(Fingerprint, (a, b, i))

8: Face ← Inverse DCT (Coeff)

Output: Fingerprint, Face

C. Tamper Detection

As the watermark images are not static or extracted from features in the cover image, and as fingerprint images are different among individuals, it is not possible to use a similarity measure between the retrieved watermark and a model image to detect any tampering with the received image. Thus, a machine learning technique, based on Convolutional Neural Network (CNN) is proposed to learn the patterns of a fingerprint. This neural network can then be used to detect fingerprint images in the extracted watermarks, so that, if such patterns are missing, the image is considered to be tamper with.

As shown in Figure 1, the implemented CNN consists of three convolutional layers, with 128, 64 and 32 filters of 2×2 pixels size, each followed by a MaxPooling layer with 2×2-pixel filter size, to maintain accurate positioning of the detected patterns. These layers are followed by two hidden fully-connected layers, with 256 and 128 neurons with 50% dropout rate each, to avoid overfitting. The output layer consists of a single neuron, as only one output value is required, which represents the probability of the input containing a fingerprint image. All layers, except the output layer use Rectified Linear Unit (ReLU) activation function, according to the good performance and fast learning rates they provide. The sigmoid activation function is used for the neuron in the output layer, as the output is required to be in the range [0,1]. The CNN is trained using a set of images, where images that contain fingerprint images are labeled with one, while those that do not have fingerprint images are labeled with zero.
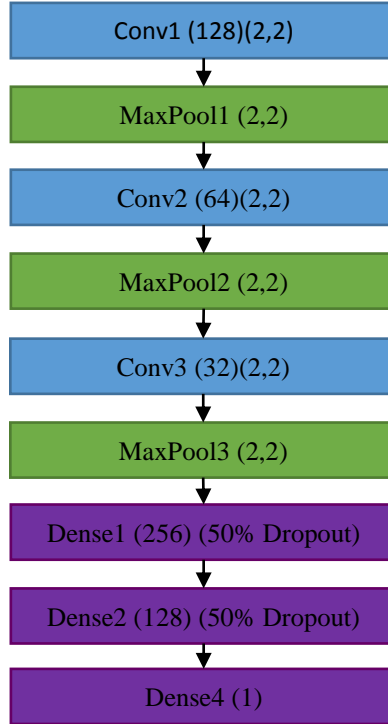
Figure 1: Structure of the fingerprint detection CNN.

III. FINGERPRINTS AND FACE IMAGES DATASETS

To evaluate the performance of the proposed methods, two fingerprint and three face images datasets are used to measure the similarity between the cover images, before and after watermarking, as well as the detection rate of the CNN. The FVC 2002DB1 and FVC 2004DB4[31] fingerprint dataset are used, as these datasets are used in earlier studies. For face images, the Indian Faces[32], the ORL Database of Faces and the FERET[33] Faces dataset are used. These datasets are selected to allow comparison between the proposed method and the state-of-the-art methods that exist in the literature. Table summarizes the contents of each of the datasets used in this study. The ORL and FERET face images dataset are combines with the fingerprint images of the FVC 2002 dataset, while the Indian Faces dataset is combined with the fingerprint images from the FVC 2002 and FVC 2004.

IV. EXPERIMENTAL SETUP AND RESULTS

All experiments are implemented using Python programming language [34], where the OpenCV library [35] is used for image processing while Keras artificial neural networks library [36] is used with Tensorflow [37] machine learning library as its backbone. The SciKit-Learn [38] library is used to calculate the performance measures of the proposed method. These experiments are conducted using an Intel® Core™ i7-7700HQ processor at 2.81GHz frequency and 16.0GB of memory running with Windows 10 Pro operating system. A GTX1080Ti Graphical Processing Unit (GPU) is used to accelerate the computations required by the CNN in the tamper detection phase.

A. EXPERIMENTAL METRICS

The performance of the proposed method can be illustrated using four aspects:

1) The distortion in the fingerprint and face images imposed by the watermarking process, as these images are required in the authentication process.
2) The tamper detection accuracy under different attacks executed against the watermarked image.
3) The reduction in the size of the data required to be transferred, when the watermarked image is used instead of communicating both images solely.
4) The complexity of the proposed method, measured by computing the time consumed by the proposed method to watermark the images, extract the original images and detect any tampering with the watermarked image.

The distortion imposed by the watermarking can be illustrated by measuring the similarity between the fingerprint image before watermarking and those extracted from the received watermarked image, and the face images before and after the fingerprint images are inserted in them. Two similarity measures are used to calculate these similarities, which are the Peak Signal to Noise Ratio (PSNR) [39] and the Structural Similarity Index Measure (SSIM) [40]. Equation (1) is used to calculate the PSNR, while the SSIM is measured using Equation (2).

$$PSNR = 20log_{10}Max - 10log_{10}MSE,$$

(1)

where,

$$MSE = \frac{1}{m \times n} \sum_{i=0}^{m-1} \sum_{j=0}^{n-1} [I(i,j) - R(i,j)]^2$$

$$SSIM = \frac{4\sigma_{IR}\overline{I}\;\overline{R}}{(\sigma_I^2 + \sigma_R^2)\left[(\overline{I})^2 + (\overline{R})^2\right]} \tag{2}$$

where,

$$\overline{I} = \frac{1}{n}\sum_{i=1}^{n} I_i, \qquad \overline{R} = \frac{1}{n}\sum_{i=1}^{n} R_i,$$

$$\sigma_I^2 = \frac{1}{n-1}\sum_{i=1}^{n}(I_i - \overline{I})^2, \quad \sigma_R^2$$

$$= \frac{1}{n-1}\sum_{i=1}^{n}(R - \overline{R})^2,$$

$$\sigma_{IR} = \frac{1}{n-1}\sum_{i=1}^{n}(I_i - \overline{I})(R - \overline{R}).$$

The tamper detection accuracy is measured by calculating the False Acceptance Rate (FAR), which represents the ratio of tampered images predicted as normal, and False Rejection Rate (FRR), which represents the ratio of untampered images predicted to be tampered with. These measures are calculated using Equation (3) and (4), respectively.

$$FAR = \frac{FP}{FP + TN} \tag{3}$$

$$FRR = \frac{FN}{TP + FN} \tag{4}$$

---

where,

TP: Untampered images predicted as untampered.

TN: Tampered images predicted as tampered.

FP: Tampered images predicted as untampered.

FN: Untampered images predicted as tampered.

B. EXPERIMENTS ASSUMPTION

In the conducted experiments, the face images in the selected dataset have dimensions of 119×92 pixels, while the fingerprint images have 200×200 pixels. All JPEG compressions are set to 90%, in order to maintain acceptable quality for the biometric authentication stage. The keys used for Arnold transformation are a=1, b=1, i=10.

C. FINGERPRINT AND FACE IMAGES SIMILARITY

The block diagram shown in Figure 3 illustrates the procedure followed to measure the similarity between fingerprint and face images. Per each individual in the dataset used for evaluation, the average PSNR and SSIM values are calculated, which are illustrated in Table
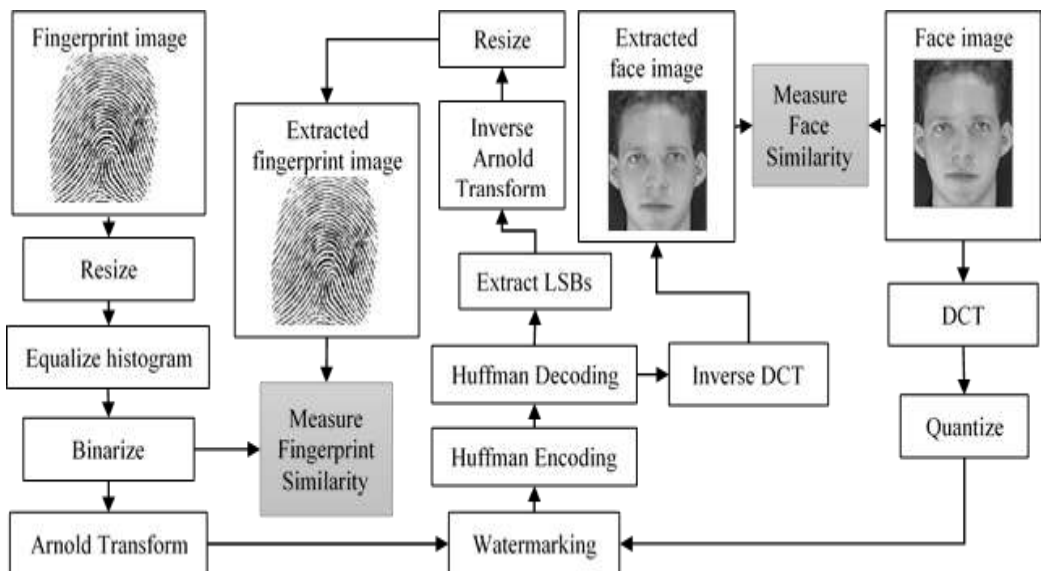
Figure 2: Fingerprint and face images similarity measurement block diagram

Individual	Face Images		Fingerprint Images	
	Average PSNR (dB)	Average SSIM	Average PSNR (dB)	Average SSIM
1	46.71	0.9983	58.23	0.9977
2	49.15	0.9994	57.42	0.9971
3	48.14	0.9988	56.86	0.9967
4	45.06	0.9967	56.77	0.9967
5	41.6	0.994	57.08	0.997
6	42.36	0.9966	57.26	0.9971
7	48.17	0.9992	57.29	0.9971
8	47.89	0.9984	57.07	0.9969
9	35.38	0.9886	56.96	0.9968
10	49.1	0.9993	57.23	0.997
11	47.91	0.9991	57.24	0.9971
12	39.79	0.9933	58.09	0.9977
13	45.98	0.9982	57.3	0.9971
14	45.69	0.9981	58.36	0.9975
15	49.12	0.9994	57.03	0.9969
16	49.18	0.9994	57.09	0.9969
17	45.26	0.9987	57.16	0.997
18	40.83	0.9926	57.67	0.9975
19	43.17	0.9975	57.08	0.997
20	48.24	0.9991	57.35	0.9972
21	43.17	0.9966	57.33	0.9971
22	49.12	0.9995	57.75	0.9974

23	45.06	0.9975	57.2	0.9971
24	44.29	0.9992	57.28	0.997
25	37.51	0.9915	57.22	0.997
26	36.99	0.9905	57.55	0.9973
27	47.83	0.9991	56.94	0.9969
28	45.86	0.9983	57.08	0.997
29	45.33	0.9985	56.76	0.9967
30	47.96	0.9993	57.73	0.9974
31	44.25	0.9987	58.15	0.9976
32	41.1	0.9959	57.37	0.9972
33	49.18	0.9995	56.66	0.9966
34	41.37	0.9993	56.8	0.9969
35	42.02	0.9944	57.22	0.9971
36	49.06	0.9994	57.44	0.9972
37	48.13	0.9988	57.04	0.9969
38	47.26	0.9982	57.3	0.9969
39	49.2	0.9994	56.31	0.9963
40	43.86	0.9959	57.38	0.9973
Overall Average:	**45.18**	**0.9974**	**57.44**	**0.9973**

The results of this experiment show that the similarity between the face images, before and after being watermarked, vary from 35.38 to 49.20 dB PSNR with an average of 45.18, while the similarity measures vary from 99.86% to 99.95%, with an average of 99.74%. Moreover, the similarity between the binarized fingerprint image prior to the watermarking and the image extracted from the watermarked image varies from 56.31dB to 58.36dB PSNR, with an average of 57.44, while the SSIM measure varies

from 99.63% to 99.77%, with an average of 99.73%. These results show that the distortion imposed by the watermarking technique is so low that it does not affect the features in the images, which are used for biometric matching. Moreover, binarizing the fingerprint image has been able to increase the similarity measures of the fingerprint images, and reduce the distortion in the face images, as less data are watermarked in them.

In comparison, the method presented by Noore et al. [14] watermarks the face image over the fingerprint image for multimodal biometric systems. This method embeds the face image in certain texture regions in the DWT of the fingerprint image, selected based on a number that is used as a secret key to decrypt the watermark data. The similarity measures of this method are 97.58%, between the original and watermarked watermark face images, and 92.59% between the cover fingerprint images, before and after adding the watermarks. These results show that the proposed method has better similarity measures, which produces more accurate biometric authentications, as the less distortion is imposed by the proposed method. This comparison also shows the use of the entire image, in the proposed method, instead of certain regions can reduce the distortion, as the density of the watermark data is reduced when the entire image is used. More comparisons to more recent techniques are shown in Table 2 to illustrate the performance of the proposed method, regarding the average PSNR and SSIM measures.

Table 2: PSNR and SSIM comparisons with the literature

Study	PSNR (dB)	SSIM
This study	51.31	0.99735
Rohit et al.[18]	42.59	0.987
Rohit et al.[19]	43.62	0.9850
Nafea et al.[20]	23.17	0.9495
Naima et al.[22]	30.00	0.989
Rohit et al.[17]	44.52	0.4998

C. TAMPER DETECTION ACCURACY

In this experiment, the fragility of the proposed watermarking technique is evaluated, alongside with the temper detection rate, using the trained CNN. First, the performance of the trained CNN is evaluated when no attack is executed against the watermarked image. Then, different attacks are executed before extracting the watermark from the image and forward it to the tamper detection method. In both

cases, the detection rate is measured, and a sample of the extracted watermarks is collected, to illustrate the performance of the tamper detection method and the fragility of the watermarking technique. Figure 4 shows the procedure followed during this experiment.
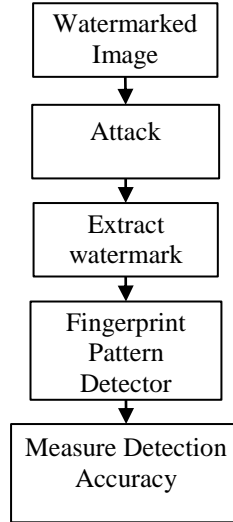
Figure 3: Tamper detection evaluation procedure.

Although the proposed watermarking method is aimed to watermark compressed images, compressing the watermarked image is one of the attacks that may be executed against it. Thus, it is important to evaluate the ability of the proposed method to detect such tampering. Moreover, attacks such as Salt & Pepper, Medial Filters and Gaussian Noise are widely used to evaluate the robustness or fragility of a watermarking technique. Thus, each of these attacks is executed on the watermarked image, before extracting the watermark information from it, using different intensities. The results of this experiment are summarized in Table 3.

Table 3: Tamper detection performance evaluation.

Attack Type	FAR	RR	Accuracy	Extracted Watermark
None	0	0	1	
Salt & Pepper (0.001)	0	0	1	
Salt & Pepper (0.002)	0	0	1	
Salt & Pepper (0.01)	0	0	1	
Salt & Pepper (0.05)	0	0	1	
Salt & Pepper (0.1)	0	0	1	
Median Filter (3x3)	0	0	1	
Median Filter (5x5)	0	0	1	
Median Filter (7x7)	0	0	1	
Median Filter (9x9)	0	0	1	
Median Filter (15x15)	0	0	1	
Gaussian Noise (0,0.01)	0	0	1	
Gaussian Noise (0,0.05)	0	0	1	
Gaussian Noise (0,0.1	0	0	1	
Gaussian Noise (0.01,0)	0	0	1	
Gaussian Noise (0.02,0	0	0	1	
Gaussian Noise (0.1,0)	0	0	1	
Gaussian Noise (0.05,0	0	0	1	

JPEG compression (10%)	0	0	1	
JPEG compression (30%)	0	0	1	
JPEG compression (50%)	0	0	1	
JPEG compression (70%)	0	0	1	
JPEG compression (90%)	0	0	1	
Average:	**0**	**0**	**1**	

The results illustrate the perfect performance of the tamper detection method, which is a result of the combination between the fragility of the watermarking technique and the accuracy of the fingerprint pattern detection method. Thus, this combination has shown the best possible performance in detecting any type of attacks that can be executed on the biometric images, stored in the models database or communicated among the different parts of the multimodal biometric authentication system. Moreover, the use of a time-sensitive encryption key with the Arnold Transformation can protect the system from any replay attacks, where messages are intercepted and replayed to the system. The images collected from watermarks in attacked images show that the LSBs are reset after each attack is executes, which creates what appears to be a random distribution of ones and zeros.

D. IMAGES SIZE REDUCTION

As the aim of the proposed method is to protect face images using the fingerprint images while reducing the size of the watermarked image, to reduce the resources consumption, this experiment evaluates the size of the resulting image. According to the JPEG standard, a quantization table is used to reduce the number of unique frequency magnitudes, so that, the size of the resulting file required to store the image is significantly reduced when Huffman Encoding is used to store those values. However, as the proposed method adjust the value of the LSBs of the values resulting from the quantization step, the resulting file is expected to be larger than the

compressed one, without watermarking, but still smaller than the original watermarked image. At a compression rate of 90%, the proposed method has produced files with 63.87% of the original, uncompressed, file size, whereas the standard JPEG compression has produced files of 53.74% of the original size. In contrast, the methods proposed in [17-19] and [23] still require storing the file using its 100% size, while the method proposed in [20] can produce files with compression rate depending on the required file size but cannot be used for tamper detection.

E. SPEED ANALYSIS

The time consumed to execute an algorithm has significant importance when the algorithm is used with real-time applications. To evaluate the effect of the dimensions of fingerprint and face images on the time required to gen

erate the watermarked image and extract them back, these images are scaled from 20% up to 200% their actual dimensions, with a 20% step size.

Figure 4: Scale of the fingerprint and face images.
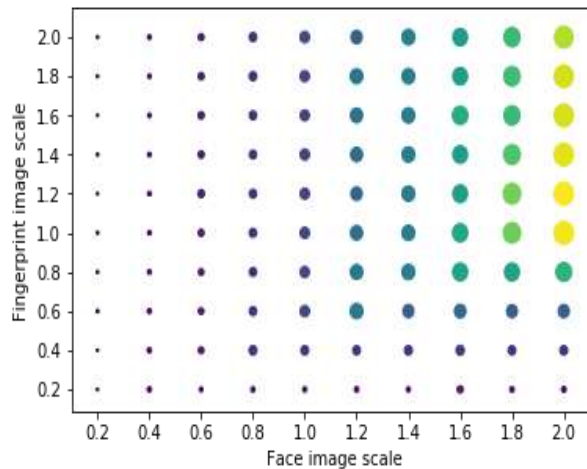
Per each scale of the face image, all possible scales of the fingerprint images are evaluated. Then, the results are summarized, in Figure 4, per each scale of the fingerprint and face images. The minimum time consumed by the proposed watermarking algorithm, to watermark and extract the images, is 0.45mS, while the maximum time is 39mS. Moreover, the graph show that the

execution time is increased only when both the fingerprint and face images have larger dimensions.

V. CONCLUSION

This paper presents a fragile watermarking technique that combines the LSB watermarking method and DCT-based compression, to protect images communicated by multimodal biometric authentication systems. The proposed method watermarks the fingerprint image over the face image, so that, any tampering with the image causes the loss of the watermark. The use of the fingerprint image as the watermark has been able to reduce the size of the data communicated in the authentication system, as both images are transferred in a single watermarked image. However, the use of a dynamic watermark that is not extracted from features in the cover image imposes the challenge of detecting tamper in the received image. Thus, a convolutional neural network is trained to recognize patterns in fingerprint images, so that, is the watermark extracted from the received image does not have such patters, the image is considered to be tampered with. The proposed method has shown perfect tamper detection rate, with very high similarity between the fingerprint and face images before being watermarked and after being extracted from the watermarked image and significant reduction in the size of the communicated data. The method has also shown very low time consumption in embedding the fingerprint image in the face image and extracting these images upon arrival, where the execution time has increased only when the dimensions of both images are increased.

In future work, the distortion imposed by the fingerprint watermark on other biometric images, such as iris, is going to be evaluated. As iris images are of smaller size and sharper details, compared to face image, the watermarking technique may impose a larger distortion on such images. However, the literature shows that the use of fingerprint and iris biometric is rarely combined together, as both of them cannot be collected passively.

REFRENCE

[1] S. A. Chaudhry, K. Mahmood, H. Naqvi, and M. K. Khan, "An improved and secure biometric authentication scheme for telecare medicine information systems based on elliptic curve cryptography," *Journal of Medical Systems,* vol. 39, no. 11, p. 175, 2015.

[2] M. Nagatomo, Y. Kita, K. Aburada, N. Okazaki, and M. Park, "Implementation and user testing of personal authentication having shoulder surfing resistance with mouse operations," *IEICE Communications Express,* vol. 7, no. 3, pp. 77-82, 2018.

[3] N. K. Ratha, J. H. Connell, and R. M. Bolle, "Enhancing security and privacy in biometrics-based authentication systems," *IBM systems Journal,* vol. 40, no. 3, pp. 614-634, 2001.

[4] M. Sajjad *et al.*, "Mobile-cloud assisted framework for selective encryption of medical images with steganography for resource-constrained devices," *Multimedia Tools and Applications,* vol. 76, no. 3, pp. 3519-3536, 2017.

[5] R. Hamza, K. Muhammad, Z. Lv, and F. Titouna, "Secure video summarization framework for personalized wireless capsule endoscopy," *Pervasive and Mobile Computing,* vol. 41, pp. 436-450, 2017.

[6] K. Muhammad, M. Sajjad, I. Mehmood, S. Rho, and S. W. Baik, "Image steganography using uncorrelated color space and its application for security of visual contents in online social networks," *Future Generation Computer Systems,* 2016.

[7] M. M. Yeung and F. Mintzer, "An invisible watermarking technique for image verification," in *Image Processing, 1997. Proceedings., International Conference on*, 1997, vol. 2, pp. 680-683: IEEE.

[8] N. Li, W. Du, and D. Boneh, "Oblivious signature-based envelope," *Distributed Computing,* vol. 17, no. 4, pp. 293-302, 2005.

[9] A. Shehab *et al.*, "Secure and robust fragile watermarking scheme for medical images," *IEEE Access,* vol. 6, pp. 10269-10278, 2018.

[10] R. Snelick, U. Uludag, A. Mink, M. Indovina, and A. Jain, "Large-scale evaluation of multimodal biometric authentication using state-of-the-art systems," *IEEE transactions on pattern analysis and machine intelligence,* vol. 27, no. 3, pp. 450-455, 2005.

[11] J. Wayman, A. Jain, D. Maltoni, and D. Maio, "An introduction to biometric authentication systems," in *Biometric Systems*: Springer, 2005, pp. 1-20.

[12] M. O. Oloyede and G. P. J. I. A. Hancke, "Unimodal and multimodal biometric sensing systems: a review," vol. 4, pp. 7532-7555, 2016.

[13] T. Sim, S. Zhang, R. Janakiraman, and S. Kumar, "Continuous verification using multimodal biometrics," *IEEE transactions on pattern analysis and machine intelligence,* vol. 29, no. 4, pp. 687-700, 2007.

[14] A. Noore, R. Singh, M. Vatsa, and M. M. Houck, "Enhancing security of fingerprints through contextual biometric watermarking," *Forensic Science International,* vol. 169, no. 2-3, pp. 188-194, 2007.

[15] T. Hoang, D. Tran, and D. Sharma, "Remote multimodal biometric authentication using bit priority-based fragile watermarking," in *Pattern*

Recognition, 2008. ICPR 2008. 19th International Conference on, 2008, pp. 1-4: IEEE.

[16] M. Vatsa, R. Singh, A. Noore, M. M. Houck, and K. Morris, "Robust biometric image watermarking for fingerprint and face template protection," *IEICE Electronics Express,* vol. 3, no. 2, pp. 23-28, 2006.

[17] R. Thanki and K. Borisagar, "Multibiometric Template Security Using CS Theory–SVD Based Fragile Watermarking Technique," *WSEAS Transactions on Information Science and Applications,* vol. 12, pp. 1-10, 2015.

[18] R. Thanki and K. Borisagar, "Biometric watermarking technique based on cs theory and fast discrete curvelet transform for face and fingerprint protection," in *Advances in signal processing and intelligent recognition systems*: Springer, 2016, pp. 133-144.

[19] R. Thanki and K. Borisagar, "Biometric Image Protection Using Compressive Sensing and DCT based Watermarking Technique," in *proceedings of RK University's First International Conference on Research & Entrepreneurship (ICRE–2016)*, 2016, pp. 1239-1248.

[20] O. Nafea, S. Ghouzali, W. Abdul, and E.-u.-H. Qazi, "Hybrid multi-biometric template protection using watermarking," *The Computer Journal,* vol. 59, no. 9, pp. 1392-1407, 2016.

[21] J. Hämmerle-Uhl, K. Raab, and A. Uhl, "Watermarking as a means to enhance biometric systems: A critical survey," in *International Workshop on Information Hiding*, 2011, pp. 238-254: Springer.

[22] N. Bousnina, S. Ghouzali, M. Mikram, and W. Abdul, "DTCWT-DCT watermarking method for multimodal biometric authentication," in *Proceedings of the 2nd International Conference on Networking, Information Systems & Security*, 2019, p. 75: ACM.

[23] B. Ma, Y. Wang, C. Li, Z. Zhang, and D. Huang, "Secure multimodal biometric authentication with wavelet quantization based fingerprint watermarking," *Multimedia tools and applications,* vol. 72, no. 1, pp. 637-666, 2014.

[24] J.-F. Mao *et al.*, "Research on watermarking payload under the condition of keeping JPEG image transparency," *Multimedia Tools and Applications,* vol. 76, no. 6, pp. 8423-8448, 2017.

[25] L. Dong, Q. Yan, Y. Lv, and S. Deng, "Full band watermarking in DCT domain with Weibull model," *Multimedia Tools and Applications,* vol. 76, no. 2, pp. 1983-2000, 2017.

[26] G. K. Wallace, "The JPEG still picture compression standard," *IEEE transactions on consumer electronics,* vol. 38, no. 1, pp. xviii-xxxiv, 1992.

[27] S. Bayram, H. T. Sencar, and N. Memon, "Efficient sensor fingerprint matching through fingerprint binarization," *IEEE Transactions on Information Forensics and Security,* vol. 7, no. 4, pp. 1404-1413, 2012.

[28] C. De Boor, C. De Boor, E.-U. Mathématicien, C. De Boor, and C. De Boor, *A practical guide to splines*. Springer-Verlag New York, 1978.

[29] L. Wu, J. Zhang, W. Deng, and D. He, "Arnold transformation algorithm and anti-Arnold transformation algorithm," in *Information Science and Engineering (ICISE), 2009 1st International Conference on*, 2009, pp. 1164-1167: IEEE.

[30] A. M. Najih, S. A. R. Al-Haddad, A. R. Ramli, and S. J. Hashim, "A New Colour Image Watermarking Technique Using Special Domain," in *2015 5th International Conference on IT Convergence and Security (ICITCS)*, 2015, pp. 1-5: IEEE.

[31] D. Maltoni, D. Maio, A. K. Jain, and S. Prabhakar, *Handbook of fingerprint recognition*. Springer Science & Business Media, 2009.

[32] V. J. h. v.-w. c. u. e. v. I. Jain, "" The indian face database," 2002," 2002.

[33] P. J. Phillips, H. Moon, P. Rauss, and S. A. Rizvi, "The FERET evaluation methodology for face-recognition algorithms," in *Proceedings of IEEE Computer Society Conference on Computer Vision and Pattern Recognition*, 1997, pp. 137-143: IEEE.

[34] M. F. Sanner, "Python: a programming language for software integration and development," *J Mol Graph Model,* vol. 17, no. 1, pp. 57-61, 1999.

[35] G. Bradski and A. Kaehler, "OpenCV," *Dr. Dobb's journal of software tools,* vol. 3, 2000.

[36] F. Chollet, "Keras: The python deep learning library," *Astrophysics Source Code Library,* 2018.

[37] M. Abadi *et al.*, "Tensorflow: a system for large-scale machine learning," in *OSDI*, 2016, vol. 16, pp. 265-283.

[38] F. Pedregosa *et al.*, "Scikit-learn: Machine learning in Python," *Journal of machine learning research,* vol. 12, no. Oct, pp. 2825-2830, 2011.

[39] C. Jinimole and A. Harsha, "Comparative Study of Different Enhancement Techniques for Computed Tomography Images," *World Academy of Science, Engineering and Technology, International Journal of Medical, Health, Biomedical, Bioengineering and Pharmaceutical Engineering,* vol. 11, no. 9, pp. 524-527, 2017.

[40] Z. Wang and A. C. Bovik, "A universal image quality index," *IEEE signal processing letters,* vol. 9, no. 3, pp. 81-84, 2002.

Effect of Nb addition on the grain growth of annealed high Mn austenitic steel structure

Hassan Zaid[1], Hassan Haji[2], Jamal Khalil[2]

Faculty of Engineering, Gahrayn University

hassan.zaid@gu.edu.ly

الملخص

يهدف البحث الى دراسة تأثير إضافة النيوبيوم على خاصية نمو الحبيبات في البنية المجهرية لسبائك الصلب الاستنيتي العالي المنجنيز المعالج حراريا. اختيرت السبيكة Fe30Mn محتوية على نسب مختلفة من عنصر النيوبيوم، حيث تم تقسيم العينات الخاضعة للدراسة الى مجموعتين. سبائك منخفض النيوبيوم من 0.05 الى 0.4% واخرى عالية النيوبيوم بنسب من 0.6 الى 1%. أجريت المعالجة الحرارية للعينات في درجة حرارة كافية لاذابة النيوبيوم واعلى من درجة اعادة التبلر 1200°C ولفترات زمنية من 2 الى 60 دقيقة. خلص البحث الى ان النيوبيوم يعمل على عرقلة نمو الحدود الحبيبية ويتضح ذلك من خلال الحجم الحبيبي الصغير كلما زادت نسبة النيوبيوم في السبيكة. هذا الاستنتاج يوضح تاثير النيوبيوم نتيجة لتأثير عنصر المنجنيز على إذابة النيوم في طور الاستيت. إتضح من نتائج البحث التطابق الواضح بين النتائج المعملية والنتائج النظرية لقياس حجم الحبيبات عند إعتماد ثابت مقارنة n=2 وان الفارق في حجم الحبيبات ليس نتيجة لتأثير النيوبيوم فحسب بل ايضا نتيجة لتأثير عنصر المنجنيز في إذابة النيوبيوم في الاستتيت.

الكلمات المفتاحية: صلب TWIP، نمو الحبيبات، مودل رياضي، ذوبانية عنصر النيوبيوم.

ABSTRACT

An investigation has been carried out to study the effect of Niobium (Nb) addition on the grain growth characteristics of Fe30Mn –TWIP steel alloy. The studied steel samples have been divided in to two groups which are low-Nb (0.05-0.4 Nb wt%) group and high Nb one (0.6 and 1Nb wt%). All samples were heated at dissolution temperature just above the recrystallization stop temperature of 1200°C at different period of times. It has been found that simultaneous addition of Nb inhibits the austenitic grain growth markedly. However, Significant grain refinement was observed in high Nb group. This indicates a stronger grain boundary pinning effect due to

the effect of Mn on the Nb solubility. The comparison between the experimental values of grain size at 1200°C and empirical modelling using ***n = 2*** shows a reasonable agreement. variation of grain growth behavior could be due to the effect of Manganese on Nb solubility in austenite.

Keywords: TWIP steel, grain growth, empirical modelling, Nb solubility.

1. INTRODUCTION

High Manganese steels have full austenite stability at room temperature and low stacking fault energy. Thus variations in carbon and nitrogen levels in solution do not impact significantly on the stable phase [1]. The austenite grain size of high Mn steel is an important factor which controls the transformation characteristics and, thus, influences the resulting microstructure and mechanical properties [2]. Due to its retarding effect, Nb has been used to control the austenite grain growth during steel heat treatment, [1]. Manohar, P. [3], studied the effect Nb on the grain growth of austenite in high Mn steels during heat treatment and reported that increasing of Nb content retards the γ phase transformation and raises the Ar3 temperature during heat treatment.

Nb affects the grain boundary migration by the segregation of Nb solutes which can introduce a frictional drag on the moving boundary. Presence of Nb second phase particles can also decreases the grain boundary area and, hence, the overall grain boundary energy, thus producing a grain boundary pinning effect [4]. Austenite grain boundary pinning is particularly effective and important for the toughness of steels in which the final properties are obtained by quenching and tempering.

In this work, different Nb content Fe30Mn alloy, has been austenitized at 1200°C for different times in order to study the grain growth (G.G) behavior of Fe30Mn alloy microstructure. This work also uses a mathematical model from previous study [4], to explain and understand the effect of Nb on the (G.G) of annealed austenitic steel.

2. Experimental Part

The materials used in this work were (2.7x30x120) mm **of 73% hot rolled**

plate samples of Fe30Mn and other six Nb-Fe30Mn levels with chemical composition given in Table 1.

Table 1: Chemical Composition Of The Experimental Steels By (wt%)

Alloy ID	Mn W%	Nb W%	C Wt%	N Wt%
Fe30Mn	29.2	0.0001	0.002	0.0026
0.05Nb	29.7	0.044	0.002	0.005
0.1Nb	29.9	0.078	0.004	0.007
0.2Nb	30.02	0.18	0.008	0.01
0.4Nb	30.1	0.46	0.008	0.011
0.6Nb	30.2	0.62	0.013	0.011
1Nb	30.2	1.0	0.021	0.012

All isothermal grain growth tests were performed on materials presented in Table 1 (as two groups; 0.05Nb, 0.1Nb, 0.2Nb and 0.4Nb wt% as group1, 0.6Nb and 1Nb wt% as group 2) using a muffle furnace at 1200°C for 2, 10, 30 and 60 minutes. A 1200°C annealing temperature has been selected as a temperature at which recrystallization was completed [5,6]. The samples were prepared using standard metallographic techniques and etched in saturated aqueous 7% solution of sodium Meta bi-sulphate for further optical observation and scanning electron microscopy. To obtain the average grain size, linear intercept method has been implemented on the SEM images and average grain size was calculated.

3. RESULTS AND DISCUSSION

3.1 Microstructure investigation

3.1.1 Fe30Mn alloy samples

Microstructure of Fe30Mn annealed samples exhibits fully recrystallized equaixed austenite grains with variety of annealing twins at 1200°C for 2 minutes. As the dissolution time increases up to 30 min, the grain size increases. This can be explained by the reduction in the surface

energy. Extensive grain growth was observed in Figure 1C and that could be attributed to few grains growth dramatically in expense of smaller recrystallized grains in order to reduce the grain boundary energy.
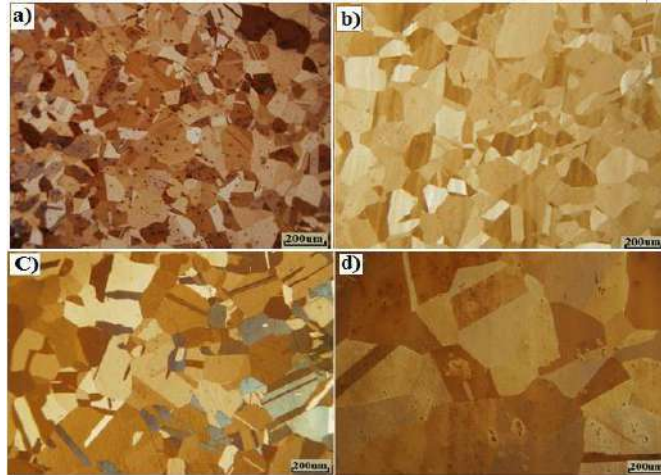
Figure 1: An optical micrograph of annealed Fe30Mn at 1200°C for different times; a) 2 minutes, b) 5 minutes, c) 10 minutes and d) 30 minutes.

3.1.2 Nb-Fe30Mn alloy samples

Annealing at 1200°C was performed for all Nb-Fe30Mn alloys and recrystallization occurred at short times. For the low-Nb group alloys (0.05-0.4Nb wt%), high recrystallization fraction was seen in the annealed structure at 1200°C for two minutes and was fully recrystallized when all samples were held for 5 minutes. Grain growth was seen with increasing time (Figure 2, Figure 3 and Figure 4. From figures, This recrystallization and grain growth behavior is due to the difference in the presence of Nb precipitates.
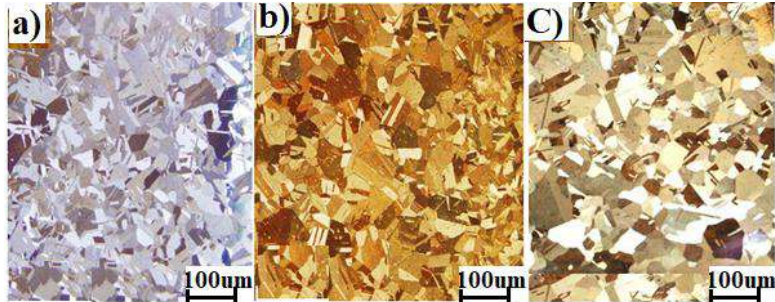
Figure 2: Optical micrographs show grain growth of grade 0.05Nb annealed at 1200°C for a) 5, b) 10, and C) 30 minutes.
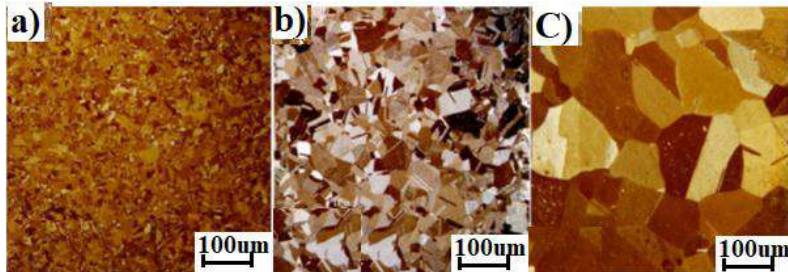
Figure 3: Optical micrographs represent grain growth of 0.1Nb samples annealed at 1200°C for a)5, b)10, and c) 30 minutes.
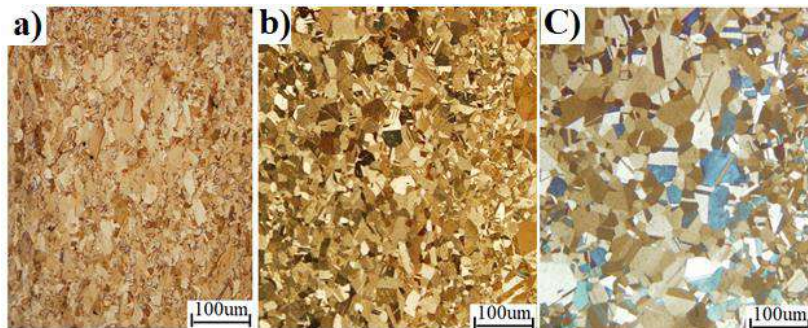
Figure 4: Optical micrographs of annealed 0.2Nb sample at 1200°C for a) 5, b) 10 and C) 30 minutes.

High Nb samples show partially recrystallized microstructures at soaking times of 2 minutes and 5 minutes Figure 5. This can be explained by the incomplete dissolution of Nb particles and that Nb carbides volume fraction

حقوق الطبع محفوظة لمجلة غريان للتقنية

were more effective in retarding recrystallization.
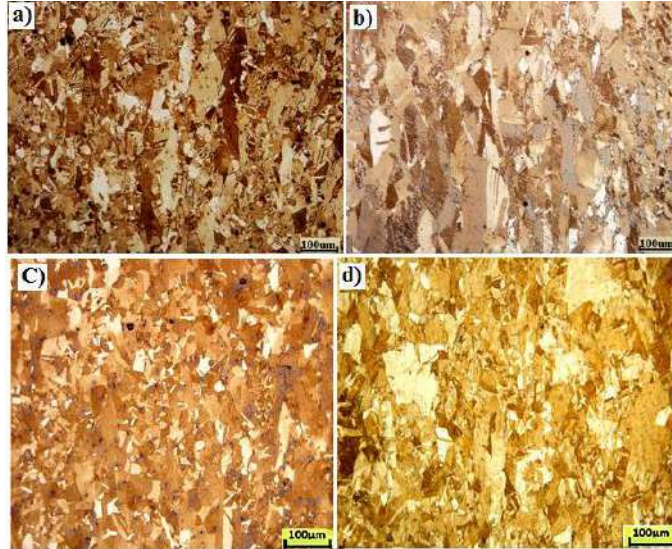
Figure 5: Optical microstructure of annealed at 1200◦C a) 0.4Nb for 2 min, b)1Nb for 2 min, C) 0.4Nb for 5 min, and d) 1Nb for 5 min.

However, there was a difference in grain growth in the annealed high Nb studied samples. As Nb increased, the grain growth decreased and for the 1%Nb shows less growth even at longer time as seen in Figure 6.
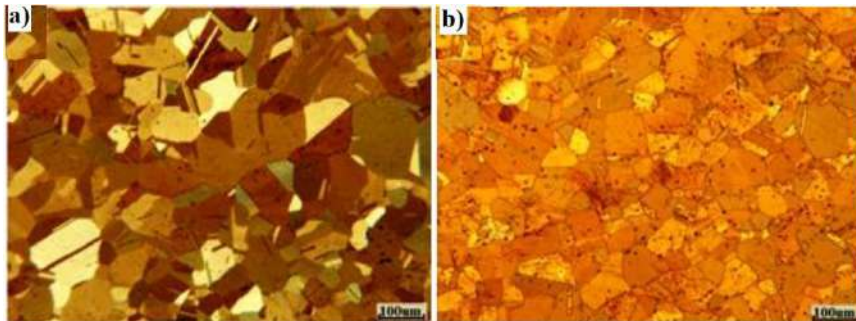
Figure 6: An optical micrograph of annealed a) 0.4Nb for 10 min, b) 1% Nb for 30 minutes.

3.2 Grain Size Measurements

Line interceot method was used to calculate the grain size of the annealed grains and the results have been cheked by ImagJ software. Five optical micrographs have been taken for each annealing time and the average grain size results were tabulated as shown in Table 2.

Table 2: Grain size measurement of the studied alloys at 1200°C

| Annealing time (min)	Grain Size (μm) at 1200°C						
	Fe30Mn	0.05Nb	0.1Nb	0.2Nb	0.4Nb	0.6Nb	1Nb
0	152.4	136.8	128.7	120.2	117.6	63.3	33.8
5	218.1	155.9	141.3	134.2	130.3	77	40
10	265.8	184.6	180.2	174.6	166.8	88.6	51.6
30	425.3	246.5	239.6	224.2	216.5	106.8	83.8
60	538.9	359.1	328.2	294.3	271.6	133.2	127

Data presented in Table 2 indicates distinct stages in grain growth of Nb-Mn steel of different Nb contents. It also shows the effect of Nb on austenite grain growth which also affected by the presence of high Mn content.

4. DISCUSSION

In a comparison of the grain growth behavior of the two alloy groups, it can be observed that the grain sizes of the lower Nb alloys are always the largest, while those in alloy containing 6Nb and 1Nb are the finest. Figure 7, plots the grain size as a function of time. The base grade shows a grain size increase of about 3.5 times over the 60 minutes of annealing and the Nb grade displays a coarsening ratio of similar size (~4 times). Overall, the grain size is seen to increase by 2.5 - 4 times during annealing for 60 minutes at 1200°C with no grain boundary pinning force due to influence of Nb on this parameter. However, the different starting grain sizes means that a further analysis is required; the starting grain size controls the driving pressure for grain growth.

حقوق الطبع محفوظة لمجلة غريان للتقنية
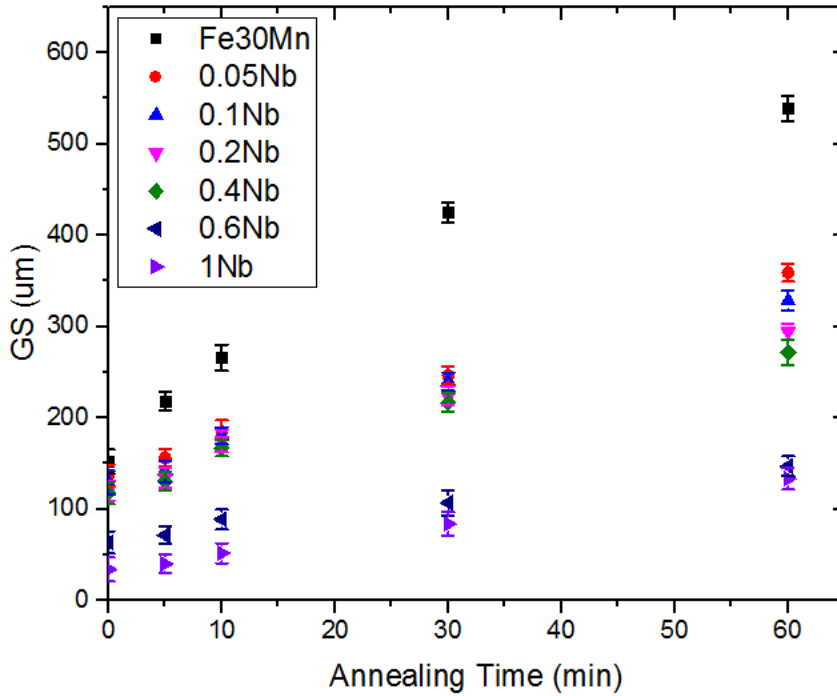
Figure 7: Grain size as a function of annealing time at 1200°C.

Grain growth analysis

The aim of this section is to model the grain growth behavior of the studied alloys in order to understand the Nb effect on the annealing behavior at 1200°C. Grain growth is typically described using the equations below:

$$D^n - D_0^n = K_1\, t$$

$$K_1 = k\, exp\left(-\frac{Q}{RT}\right) = \frac{D^n - D_0^n}{T}$$

where **D0** is the initial grain size (size of the grains at 1200°C/2 min in the present case) and **D** is the final grain size, **K1** is a rate constant (μm2/sec) that depends on the temperature, activation energy for grain growth **Q** and a constant **k.** The comparison between the experimental values of grain size at 1200oC and empirical modelling using **n = 2** shows reasonable agreement as shown in Figure 8. And the reason behind choosing the value of time exponent (**n = 2**)is that the assumption of the effect of only solute drag on

grain growth and very low of pinning effect due to the coarse particles and their low fraction as found in earlier work [4,7].
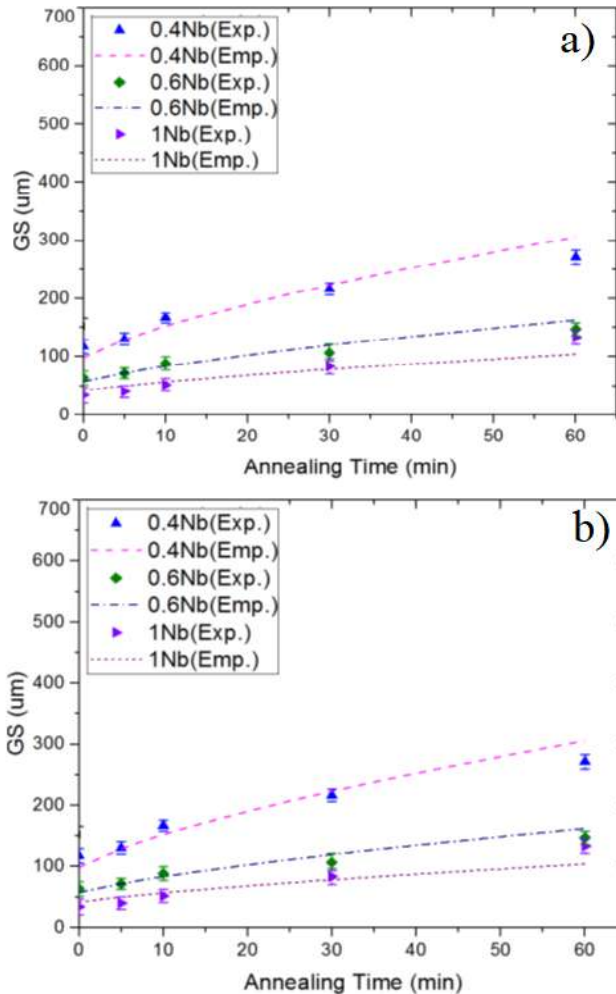
Figure 8: Comparison between experimental (Exp.) grain growth and empirical (Emp.) equation of grain growth of the studied alloys at 1200°C for the studied alloys (all divided in a) and b) graphs)

The experimental grain growth rate constant , K1, is plotted in Figure 9. It clearly shows the effect of Nb on grain growth. Over the range studied, Nb drops the rate of grain growth by over an order of magnitude. Interestingly, the addition of 0.05% Nb drops the rate by a factor of ~2. The rate constants

for the 0.6 and 1.0Nb grades are particularly low, perhaps reflecting the presence of Nb(C,N)
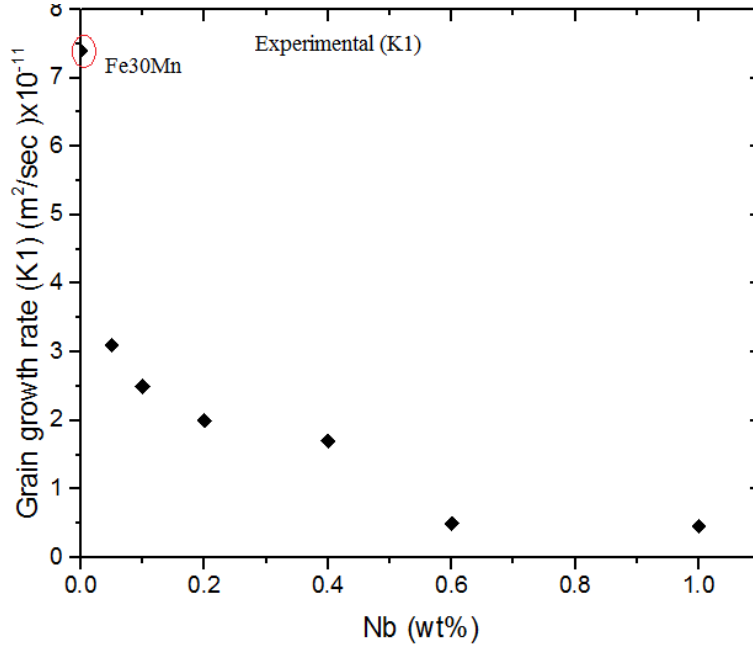
Figure 9: The effect of Nb on grain growth rate (K1) at 1200°C as experimental data results.

5. CONCLUSION

1- Microstructure investigation shows a grain growth of Fe30Mn alloy is a behavior of an austenitic microstructure where grain size increased as annealing time was increased.

2- The effect of Nb in low-Nb Fe30Mn alloys was clearly observed by the grain size measurements.

3- Grain growth of high-Nb Fe30Mn samples was less than that of low-Nb ones.

4- Overall grain growth of the studied alloys can be concluded as the lower Nb content alloy (Fe30Mn0.05Nb) was about 3.5 times faster than that of the growth in high-Nb content one

5.Austenite grain growth model provided satisfactory prediction of austenite

grain size at high austenising temperature of 1200C.

6. Excessive grain growth behavior was observed in the Fe30Mn alloy. This indicates that the driving force for grain growth is the reduction in the grain boundary energy.

References

[1] W. Bleck, C. Haase,"Physical Metallurgy of High Mn Steel", Journal of Metals, 2019,9, Page 1053.

[2] H. Adrian and F. Pickering, "Effect of titanium additions on austenite grain growth kinetics of medium carbon V–Nb steels containing 0008–0018%N", Journal of Materials Science and Technology, 7, (2), page 176-182

[3] Manohar, p., Grain Growth and Continuous cooling transformation behaviour of austenite in Ti-Nb-Mn-Mo microalloyed steel. PhD Thesis - Wollongong University 1997.

[4] H. zaid, "Effect of Nb addition on the behavior of Fe30nMn TWIP steel" Deakin University-Australia, 2017, page 122-145

[5] Killmore, P.M.a.C., Grain Growth Predictions in Microalloyed Steels. ISIJ International. Vol. 36 1996. 36(2): p. 194-200.

[6] H. Zaid, "SOLUBILITY AND PRECIPITATION OF Nb IN AN ANNEALED Fe-30Mn STEEL", Journal of Engineering Research (University of Tripoli, Libya) Issue (29) March 2020.

[7] Fortes, M.A., Grain growth kinetics- the grain exponent Materials Science Forum, 1992. 94-96: p. 319-324.

The reasons that cause changing of Earth daytime by increasing and decreasing velocity of rotation around its self

Mahmood Salem Dhabaa

Geology department, faculty of science, Gharyan University

الملخص

سرعة دوران الأرض حول نفسها تتغير بسبب العديد من الأسباب والتي تؤدي الي تغيير في طول زمن اليوم. الأسباب التي تعمل على تغيير في سرعة دوران الأرض يمكن تقسيمها الي عاملان رئيسيين هما: تغيرات داخلية لا يمكن ملاحظة لأنها تحدث تحت القشرة الأرضية، بالإضافة الي العامل الاخر الذي يعرف بالتغيرات الخارجية وهي عبارة عن تحولات طبيعية تكون فوق سطح الأرض. كلا العاملين السابقين يعمل علي زيادة او خفض طول الزمن اليومي الأرضي. بالنسبة للعامل الأول يتمثل في عوامل طبيعية مثل الزلازل وحركة الصهارة وتكثّفها داخل منطقة الوشاح **(mantle)** والنواة وغيرها، اما التغيرات الخارجية فتتجلى في ظواهر طبيعية مثل المد والجز البحري وذوبان الجليد القطبي وغيرها. أخيرا، زمن تغير طول اليوم الأرضي لا يتعدى سوي بعض الثواني من سنة الي اخري، ولكن يمكن ان تكون لها قيمة كبيرة على فترات زمنية طويلة.

Abstract:

Earth velocity changes under many reasons. They cause variations in the length of daytime. These reasons are; interior changes, which usually occur during events that tend to speed up Earth's rotation slightly but noticeably, and Outward changes, where material that was typically at one point at a higher elevation on Earth surface falls down to be at a lower point. The first reason may show in several figures like earthquake and condensing core of earth. On the other hand, tide, melting glacier poles, and changing weather they cause the other reason. The amount of time that increasing or decreasing in a day until now do not exceed few seconds, but on the massive scale of time as the age of earth it becomes important value.

Introduction:

Earth is unique known planet. It has a plenty of water. Our world has a moon, atmospheres, ice, and even oceans. Additionally, Earth has the right combination to sustain life. Earth's oceans cover about 70 percent of the

planet's surface with an average depth of 4 kilometers. Fresh water exists in liquid form in lakes and rivers and as water vapor in the atmosphere, which causes changing on the weather of the Earth in atmospheric layers. Earth has multiple layers. These layers are crust, mantle, and core **[3],[9]**.

The upper layer is crust. It is divided into group of huge plates that float on fluid material of mantle that placed under this layer. The plates are continually in motion. Earthquakes occur when these plates friction or collide against each other. Mountains form when the plates collide and deep trenches form when one plate slides opposite another plate. Plate tectonics is the theory explaining the motion of these plates. The mantle under the crust is about 2,890 km deep. It is composed mostly of silicate rocks rich in magnesium and iron. Intense heat causes the rocks to rise. They then cool and sink back down to the core. This convection steams is thought to be what causes the tectonic plates to move. When the mantle pushes through the crust, volcanoes erupt. At the center of the Earth is the core, which has two parts. The solid, inner core of iron has a radius of about 1,220 km. It is surrounded by a fluid outer core composed of a nickel-iron mixture. The outer core is about 2,180 km thick. The inner core revolves at a different speed than the rest of the planet. This creates Earth's magnetic field **[5],[12]**.

Scientists who assess the planet's weather see convinced evidence that Earth has been getting warmer, in some cases quickly. Most of them believe that human activity, in particular the burning of fossil fuels causes increasing the greenhouse gases in the atmosphere. Consequently, the global warming has been started. In the past decade, scientists started recording high average annual surface temperatures roughly every year. They have been observing other signs of change all over the planet: in the distribution of ice, and in the salinity, levels, and temperatures of the oceans **[2],[8]**.

Issac Newton's laws of motion describe how winds and air pressure quantities are related to the Earth's rotation rate. This leads to a change in the length of day. It is named also as polar motion, or Earth wobble).

To understand the concept of angular momentum, imagine the Earth spinning in space. Given Earth's overall mass and its rotation, it contains a certain amount of angular momentum. When an additional force acting at a distance from the Earth's rotational axis occurs, referred to as a torque, such as changes in surface winds, or the distribution of high and low pressure patterns, especially near mountains, it can act to modify the rate of the Earth's spin or even the direction of the revolving axis.

Because of the law of "conservation of angular momentum," small but detectable changes in the Earth's rotation and those in the rotation of the atmosphere are linked. The conservation of angular momentum is a law of physics that states the total angular momentum of a rotating object with no outside force remains constant regardless of changes within the system. An example of this principle occurs when a skater pulls his or her arms inward during a spin. This changing in the mass distribution of one nearer the rotation axis is reducing the "moment of inertia," and speeds up (increasing the skater's spin); because the moment of inertia goes down, the spin rate must increase to keep the total angular momentum of the system unchanged. "The key is that the sum of the angular momentum (push) of the solid Earth plus atmosphere system must stay constant unless an outside force (torque) is applied," Salstein said. "So if the atmosphere speeds up (stronger westerly winds) then the solid Earth must slow down (length-of-day increases).Also if more atmosphere moves to a lower latitude (further from the axis of rotation), and atmospheric pressure increases, it also gains angular momentum and the Earth would slow down as well." Other motions of the atmosphere such as larger mass in one hemisphere than the other can lead to a wobble (like a washing machine with clothes off-balance) and the poles move, in accordance to the law of the conservation of angular momentum **[7],[13]**.

Methodology:

Earth velocity alterations have two main reasons that work to change it constantly. These reasons have named as inner and outer causes.

The inner effects have many shapes. Firstly, magma is condensing in the outer core layer that leading the inner core become bigger. The magma losing temperature since it has been created until now. This conduces altering magma from liquid to solid state. The solid magma combines with the inner core. Changing size of the inner core works to cause alteration in the rotational velocity of Earth. The solid core formed only between 1 and 1.5 billion years ago, and continues to grow, as the portion of the outer core solidifies over time. Then, the center of Earth is becoming more dense and stable, as more and more of the mass gets concentrated towards inner core. This is a big deal for rotation of the Earth. Consequently, the rotational speed increases to compensate for changing in the inner and outer core mass. Secondly, the convections steams in the mantle coat do varying the rotation speed of Earth. This magma steams are changing their paths and intense. Movement of plates depend on variation in magma flow. Thus, directions and

strength of magma currents are major reason that control of stronger or weaker earthquakes, and govern of number occurring earthquakes. Strongest earthquakes that have intense more than seven on Richter scale are increasing daily velocity rotation of Earth. When big earthquake happen, massive mass of mantle change distribution that cause shorting in the length of Earth day **[1],[9]**.

The outer effect also has many shapes. These reasons occur upper the Earth crust in ocean and atmosphere. Firstly, increasing and decreasing levels of ocean do variation in the rotation speed of Earth planet. Levels of oceans changing undergo moving the surrounding luminaries. The secular change in the planet's rotation is a classical topic in geophysics. It goes back some 300 years to when Sir Edmond Halley. Most of Halley's lunar acceleration was only apparent. It was actually the earth's rotation slowing down. The larger effect is the earth's rotational braking. This braking is caused by tidal friction. Throughout the earth's history, tidal braking has played, and it will continue to play, a dominant role in the rotation. Currently the secular change in the rotation rate increases the length of day by some 2.3 milliseconds per day per century. The other way, caused by the continual movements of the tides about the planet, produces very small but very rapid changes in rotation. These rapid changing occur at exactly the same periods as the tides themselves half-daily and daily. There are two ways that the ocean tides can cause such rapid variations. (1) As the tides move water around the globe, the moment of inertia of the earth changes by conserving the angular momentum. Therefore, the solid earth changes its rotation rate accordingly. (2) As the tidal currents slow down or speed up, they exchange angular momentum with the solid earth, which is established in the rotation rate **[4],[11]**. Furthermore, melting glacier of poles are changing levels of oceans that causes altering of daytime. When global warming has been started, temperature has raised and pole ice diminished. The melted pole ice is going to oceans and it is increasing the amount of water to new levels. This alteration in the level of oceans are effecting on the tidal movement. Then, tidal works to change velocity rotation of Earth as have been explain above. Also, "Changes in the atmosphere, specifically atmospheric pressure around the world, and the motions of the winds that may be related to such climate signals as El Niño are strong enough that their effect is observed in the Earth's rotation signal," David A. Salstein, an atmospheric scientist from Atmospheric and Environmental Research, said in 2003. El Niño is a periodic natural warming of the tropical

Pacific Ocean, while La Niña, which was observed toward the end of 2020, is a natural cooling of the same part of the Pacific **[10],[14]**. According to NOAA (National Oceanic and Atmospheric Administration), while El Niño results in a decrease in the earth's rotation rate, La Niña tends to have the opposite effect. The recent acceleration in Earth's spin has scientists talking for the first time about a negative leap second, LiveScience said. Instead of adding a leap second, which has been done several times before to make up for a slowing of the Earth's rotation, they might need to subtract one as shown in figure (1)**[6]**.
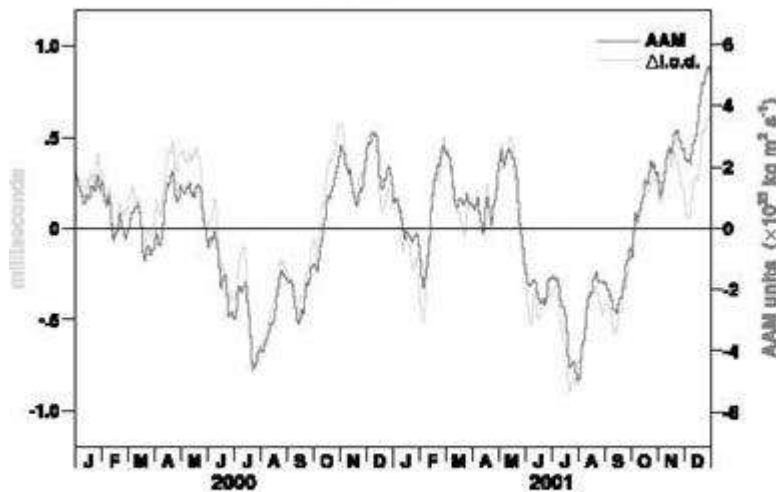
Figure (1): changing in the length of the daytime caused by El Niño and La Niña phenomena

Because of the earth's inconsistent speed, scientists in the 1950s created an atomic clock to keep precise track of time. However, as the Earth's rotation can vary, the atomic clock continued steadily ahead and the two time indicators grew farther apart. To fix that inconsistency, scientists then created UTC (Coordinated Universal Time) to help bridge the gap between Earth time and the atomic clock. However, the atomic clock continued to race ahead, so at least once every 10 years scientists added an extra leap second to

the UTC to keep them closer together. It is particularly important for things like GPS (Global Positioning System) navigation **[10].**

Conclusion:

Length of daytime is changing because many factors that have explained above. This alteration have divided to two main aspects. They are aspects increasing daytime long and they are aspects decreasing daytime long. The reasons that cause increasing daytime long are changing size of the inner core, convections steams in the mantle coat, and continual movements of the tides about the planet. On the other hand, the reasons that cause decreasing daytime long are increasing and decreasing levels of ocean and melting pole ice.

References:

[1] Alfred E. Ringwood, Origin of the Earth and Moon, Springer Science & Business Media, Germany Berlin/Heidelberg, 2012.

[2] Al Gore and Melcher Media, An Inconvenient Truth: The Planetary Emergency of Global Warming and What We Can Do About It, Rodale, USA New York 2006

[3] David Bercovici, the Origins of Everything in 100 Pages, Published by Yale University Press 2016.

[4] https://core2.gsfc.nasa.gov/ggfc/tides/intro.html

[5] https://manoa.hawaii.edu/exploringourfluidearth/node/1348

[6] https://www.livescience.com/earth-spinning-faster-negative-leap-second.html

[7] https://www.nasa.gov/centers/goddard/news/topstory/2003/0210rotation.html

[8] https://www.nationalgeographic.com/environment/article/big-thaw

[9] https://www.nationalgeographic.org/encyclopedia/core/

[10] https://www.usatoday.com/story/news/nation/2021/01/08/earth-spinning-faster-than-has-decades/6581600002/

[11] Kurt Lambeck, the Earth's Variable Rotation: Geophysical Causes and Consequences, Cambridge University Press, USA New York 2005.

[12] Pankaj Agrawal And Manish Shrikhande, Earthquake Resistant Design Of Structures, PHI Learning Pvt. Ltd, India new Delhi 2006.

[13] Richard S. Gross, The effect of ocean tides on the Earth's rotation as predicted by the results of an ocean tide model, issue 4, the American Geophysical Union, USA 1993.

[14] S. Fred Singer, Unstoppable Global Warming: Every 1,500 Years, Rowman & Littlefield, USA New York 2006.

Testing of viscosity correlations for crude oil samples

Khaled taleb

Faculty of Engineering ,Gharyan University

Khaled_taleb1970@yahoo.com

الملخص

تعتبر لزوجة النفط الخام خاصية فيزيائية مهمة لأنها تؤثر على تدفق النفط عبر الوسائط المسامية، ويمكن بشكل عام الحصول على لزوجة النفط بطريقتين، إما عن طريق إجراء قياسات تجريبية أو تقديرها بواسطة نموذج مناسب. في هذا البحث استخدم الارتباط الدقيق في حساب لزوجة النفط في ظروف التشغيل المختلفة سواء للزيوت المشبعة أو تحت التشبع. تم اقتراح العديد من الارتباطات التجريبية لحساب النفط المشبع وغير المشبع، تم الحصول على البيانات المختبرية للعثور على أفضل ارتباط، ثم تأكيد الدقة من خلال مقارنة النتائج التي تم الحصول عليها من الارتباط والنتائج الأخرى مع التجارب لعينات الزيت.

Abstract

Oil viscosity is an important physical property that controls and influences the flow of oil through porous media .Generally oil viscosity can be obtained in two ways, either by carrying out experimental measurements or estimated by a proper model. In this paper use an accurate correlation in calculating the oil viscosity at various operating conditions either for dead saturated or under saturated oils. Several empirical correlations have been suggested for calculation of the dead,saturated,and undersaturated oil, whenever laboratory data obtained are made to find a best-fit correlation ,accuracy confirmed by comparing the obtained results of the correlation and other ones with experimental for oil samples.

Keywords: undersaturated oil, dead saturated oil viscosity factor

INTRODUCTION

Viscosity is defined as the internal resistance of the fluid to flow which is related to the internal resistance or friction and is there for related to the

mobility of the fluid and is measured as the ratio of the shearing stress to the rate of shearing strain.

Dynamic viscosity

Is a measure of the internal resistance and is a tangential force per unit area required to move one horizontal plane with respect to the other at unit velocity when maintained a unit distance apart by the fluid.

Kinematic Viscosity

Is defined as the ratio of dynamic viscosity to density a quantity in which no force is involved and can be obtained by dividing the dynamic viscosity of a fluid with its mass density[1].

V = μ / ρ

Where:

V = Kinematic Viscosity

μ = dynamic viscosity

ρ = density

* Types of fluid characterizations are:

1. Newtonian (true fluids) where the ratio of shear stress to shear rate or viscosity is constant ,e.g.water,oil,etc.
2. Non-Newtonian (plastic fluids) where the viscosity is not constant.
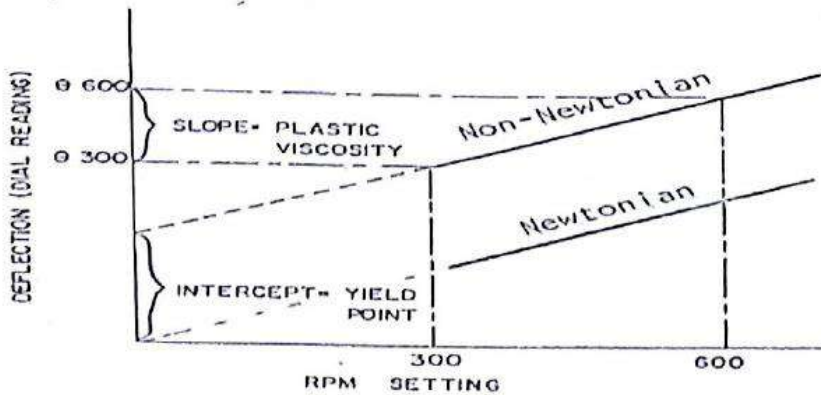
Fig (1) Types of fluid characterizations

The oil viscosity is a strong function of the temperature, pressure, oil gravity, gas gravity, and gas solubility. Whenever possible, oil viscosity should be determined by laboratory measurements at reservoir temperature and pressure. The viscosity is usually reported in standard PVT analyses. If such laboratory data are not available, engineers may refer to published correlations, which usually vary in complexity and accuracy depending upon the available data on the crude oil[2]. According to the pressure, the viscosity of crude oils can be classified

Into three categories:

• Dead-Oil Viscosity μod

The dead-oil viscosity is defined as the viscosity of crude oil at atmospheric pressure (no gas in solution) and system temperature.

• Saturated-Oil Viscosity μob

The saturated (bubble-point)-oil viscosity is defined as the viscosity of the crude oil at the bubble-point pressure and reservoir temperature.

• Undersaturated-Oil Viscosity μ

The undersaturated-oil viscosity is defined as the viscosity of the crude oil at a pressure above the bubble-point and reservoir temperature. Estimation of

the oil viscosity at pressures equal to or below the bubble-point pressure is a two-step procedure:

Step 1. Calculate the viscosity of the oil without dissolved gas (dead oil), mob, at the reservoir temperature.

Step 2. Adjust the dead-oil viscosity to account for the effect of the gas solubility at the pressure of interest.

At pressures greater than the bubble-point pressure of the crude oil, another adjustment step, i.e. Step 3, should be made to the bubble-point oil viscosity, mob, to account for the compression and the degree of undersaturation in the reservoir.

Crude oil types

Crude oil is different from field to another in appearance, and viscosity They range in color, odor, and in the properties they contain, crudes are roughly classified into three groups , according to the nature of the hydrocarbon they contain:

- Paraffin-Base crude oils

These contain higher molecular weight paraffin which is solid at related temperature, but little or no asphalile matter, they can produce high-grade lubricating oils.

- Asphaltie-Base crude oils

Contain large proportions of asphalite matter, and little or no paraffin. Some are predominantly naphthenic so yield lubricating oil that is more sensitive to temperature changes than the paraffin-base crudes.

- Mixed-Base crude oils

The gray area between the two types above .Both paraffin's and naphthenic are present, as well as aromatic hydrocarbons, most crude fit this category.

- Heavy crude oil :

Is any type of crude oil which does not flow easily. It is referred to as heavy because its density or specific gravity is higher than that of light crude oil. Heavy crude oil has been defined as any liquid petroleum with API gravity blew 10.0 °API[3-4].

Methods for estimating the viscosity:

The chosen methods are well known, accepted as potentially promising methods. They are categorized as semi-theoretical or empirical and further distinguished as predictive or correlative.

❖ Semi-theoretical methods:

Semi-theoretical are derived from a theoretical framework, but involve parameters experimentially determined.

❖ Empirical methods

Empirical methods include a wide variety of equations used throughout the industry involving constants calculated from experimental data.

Viscosity of crude oil types:

According to the pressure, the viscosity of crude oils can be classified into three categories:

1. Dead oil viscosity correlation, μ_{od}:

The dead-oil viscosity is defined the viscosity of crude oil at atmospheric pressure (no gas in solution) and system temperature. [5].

Viscosity correlations of the Dead oil:

• **The Beggs-Robinson correlation**

$$\mu_{od} = 10^x - 1$$

Where:

$$x = 1.0^{(3.0324-0.02023*°API)} \times T^{-1.163}$$

• **Labedi correlation :**

$$\mu_{od} = 10^{9.224} / (API^{4.7013} * T^{0.6739})$$

- **Petrosky and farshad correlation**

$$\mu_{od} = 2.3511*10^{7}*T^{-2.10255} * (\log API)^{(4.59388*(\log T) - 22.82792)}$$

- **Naseri correlation :**

$$\mu_{od} = 10^{(11.2699 - 4.2699x\log(API) - 2.052x\log(T))}$$

- **Kaye correlation :**

$$\mu_{od} = 10^{(T-0.65x10(2.305-0.03354xAPI)} - 1$$

- **Hossain correlation :**

$$\mu_{od} = 10^{(-0.71523xAPI+22.13766)} x T^{(0.269024xAPI-8.268047)}$$

Viscosity correlation for saturated oil:

The chew-connally correlation:

$$\mu_{ob} = (10)^{a}(\mu_{od})b$$

where:

$$a = Rs[2.2(10^{-7})Rs - 7.4(10^{-4})]$$

$$b = 0.68/10^{c} + 0.25/10^{d} + 0.062/10^{e}$$

$$c = 8.62(10^{-5})Rs$$

$$d = 1.1(10^{-3})Rs$$

$$e = 3.47(10^{-3})Rs[6,7,8].$$

2. Saturated oil viscosity correlation,μ_{od};

The saturated (bubble-point)-oil viscosity is defined as the viscosity of the crude oil at the bubble-point pressure and reservoir temperature.

Viscosity correlation for saturated oil

- **The Beggs-Robinson Correlation**

The $\mu_{ob} = a(\mu_{od})^{b}$

where:

$$a = 10.715(R_s + 100)^{-0.515}$$

$$b = 5.44(R_s + 100)^{-0.338}$$

- **The Labedi Correlation:**

$$\mu_{ob} = (10^{2.344-0.03542 \times API} \times (\mu od^{0.6447})) / (Pd^{0.426})$$

- **The Kartoatmodjo and Schmidt correlation :**

$$\mu_{ob} = -0.6821 + 0.9824 \times F + 0.0004034 \times F^2$$

where

$$F = (0.20001 + 0.8428 \times (10^{-0.000945 \times Rs} \times \mu_{od}(0.43+0.5165 \times 10^{-0.00081 \times Rs}))$$

- **The modified kartoaimodjo correlation:**

$$\mu_{ob} = 0.0132 + 0.9821 \times F - 0.005215 \times F^2$$

where:

$$F = (0.2038 + 0.8591 \times (10^{-0.000945 \times Rs} \times \mu_{od}(0.385+0.5664 \times 10^{-0.00081 \times Rs}))$$

- **Elsharkawy & Alikhan correlation:**
  $$\mu ob = a(\mu_{od})^b$$

Where:

$$a = 1241.932(Rs + 641.026)^{-1.1240}$$

$$b = 1768.841(Rs + 1180)^{-1.06622} [9,10,11].$$

3. Under saturated oil viscosity correlation, $\mu_{o:}$

The under saturated oil viscosity is defined as the viscosity of the crude oil at a pressure above the bubble-point and reservoir temperature. Under saturated oil viscosity correlation, which usually use saturated crude oil. These correlations are:

- **Beal correlation:**

$\mu_{o} = \mu_{ob} + 0.001 \times (p - pb)(0.024 \mu_{ob}{}^{1.6} + 0.038 \mu_{ob}{}^{0.56})$

- **Vasques & Beggs correlation**

$\mu_{o} = \mu_{ob}(p/pb)^{m}$

Where

$m = 2.6(p^{1.187})(10^{a})$

$a = (-3.9(10^{-5})p) - 5$

- **Khan & Ali correlation:**

$\mu_{o} = \mu_{ob} \times Exp(9.6 \times 10^{-5}(p-pb))$

- **Labedi correlation:**

$\mu_{o} = \mu_{ob} - M(1-(p/pb))$

where

$M = (10^{-2.488} \times \mu od^{0.9036} \times pb^{0.6151}) / 10^{0.01976 \times API}$

- **Kartoatmodjo & Schmidt correlation:**

$\mu_{o} = 1.00081 \mu_{ob} + 0.001127(p - pb) \times (-0.006517\mu_{ob}{}^{1.8148} + 0.038\mu_{ob}{}^{1.590}$

- **Elsharkawy & Alikhan correlation:**

$\mu_{o} = \mu_{ob} + 10^{-2.0771}(p - pb) \times (\mu_{ob}{}^{1.1279} + \mu_{ob}{}^{-0.40712} \times pb^{-0.7941}$

where:

μo = viscosity of the undersaturated oil at reservoir pressure and temperature,cp

μob = viscosity of the saturated oil at the bubble –point pressure,cp

μod = viscosity of the dead oil at 14.7 psia and reservoir temperature ,cp

p = Reservoir pressure, psi

Pb = Bubble point pressure ,psi[5].

Experiments of viscosity:

The viscosity of hydrocarbon mixtures and petroleum reservoir fluids is commonly measured by either the rolling ball viscometer or the capillary tube viscometer.

Table(1) Experimental data of samples oil

Sample #	API	T (°F)	Rs (SCF/STB)	Pb (psi)	P (psi)	μod,cp (EXP)	μob,cp (EXP)	μo,cp (EXP)
1	38	131	173	375	3015	2.57	1.43	1.82
2	39	161	521	1400	5000	1.94	0.69	0.82
3	42	167	138	340	3015	1.62	0.73	0.93
4	49	170	930	1655	5015	0.63	0.49	0.57
5	48	174	800	1560	5015	0.86	0.43	0.50
6	47	176	1762	2445	5000	0.81	0.29	0.44
7	37	184	1382	3302	4509	1.65	0.28	0.45
8	43	200	119	287	3015	1.00	0.76	0.87
9	36	210	90	495	3015	2.16	1.07	1.42
10	39	250	1738	5935	7015	3.14	0.55	0.59
11	37	258	1216	2805	5615	0.85	0.41	0.47
12	41	262	536	1525	5015	1.97	0.53	0.63
13	38	263	864	3130	5515	1.04	0.38	0.51
14	30	270	649	3002	5206	1.37	0.66	0.73
15	42	285	904	3240	4515	0.69	0.40	0.45

Results and Discussion

- **Calculation of Dead oil viscosity correlation**

Using the correlation to estimate the viscosity of dead oil, and calculate average relative Error (ARE %) and absolute average relative Error (AARE %)

ARE (%) = 1/N $\Sigma^{N}_{i=1}$ [($X_{Experiment} - X_{calculation}$)] / $X_{Experiment}$ x 100

AARE (%) = 1/N $\Sigma^{N}_{i=1}$ [($X_{Experiment} - X_{calculation}$)] / $X_{Experiment}$ x 100

i = 1,2,3……N

Table(2) Values of average relative error and absolute average relative error of dead oil

MODEL	ARE%	AARE%
Beggs-Robinson correlation	2.97	23.03
Labedi correlation	14.18	38.15
Petrosky and farshad correlation	18.92	25.81
Naseri correlation	60.17	60.17
Kaye correlation	23.56	34.86
Hossain correlation	75.27	76.51
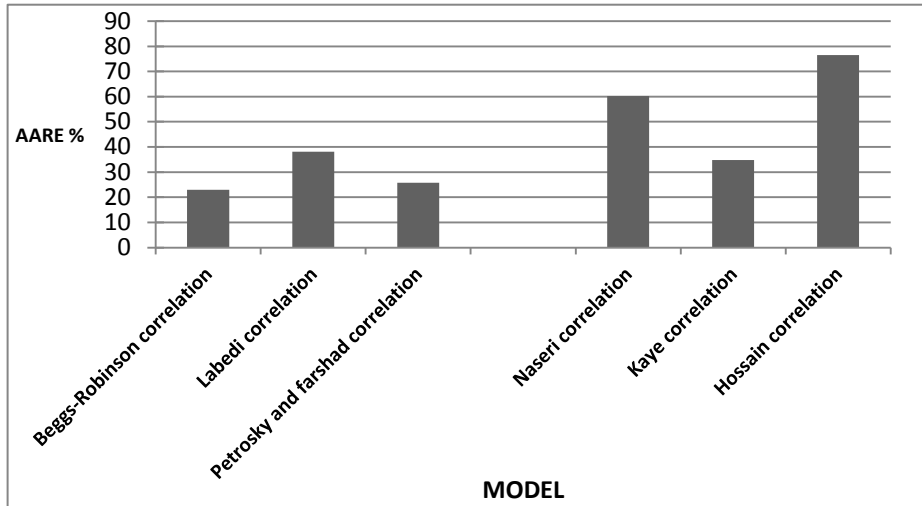
Fig(2) absolute average relative error of dead oil for every model

- **Calculation of undersaturation oil viscosity correlation**

Table(3) Values of average relative error and absolute average relative error of undersaturation oil

MODEL	ARE%	AARE%
Kartoatmodjo & Schmidt	19	25

correlation		
Elsharkawy & Alikhan correlation	8.5	24.5
Labedi correlation	11	23
Khan & Ali correlation	3.5	22.5
Beal correlation	11.5	22
Vasques & Beggs correlation	14	37
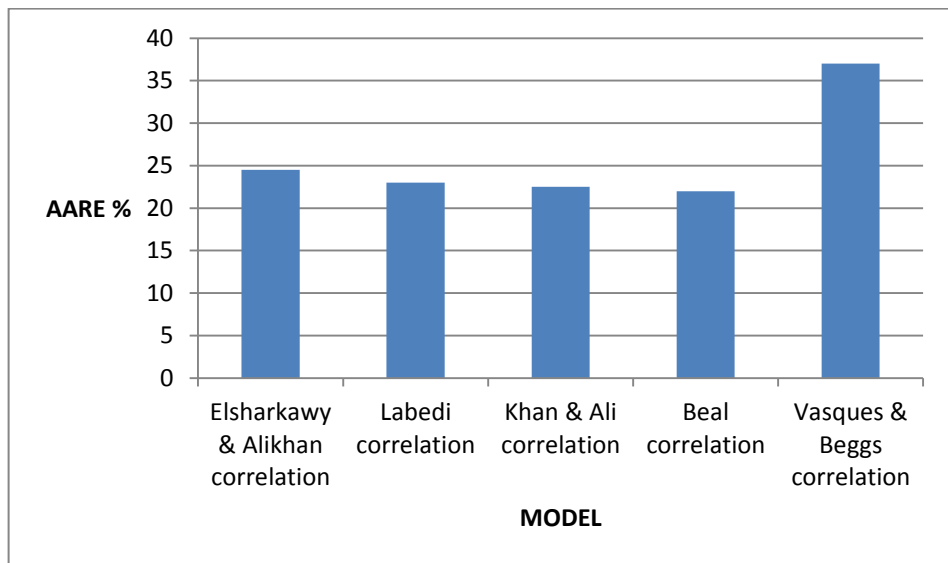
Fig(3) absolute average relative error of   undersaturation oil for every model

• **Calculation of undersaturation oil viscosity correlation**

Table(4) Values of average relative error and absolute average relative error of undersaturation oil

MODEL	ARE%	AARE%
Kartoatmodjo & Schmidt correlation	19	25
Elsharkawy & Alikhan correlation	8.5	24.5
Labedi correlation	11	23
Khan & Ali correlation	3.5	22.5

Beal correlation	11.5	22
Vasques & Beggs correlation	14	37
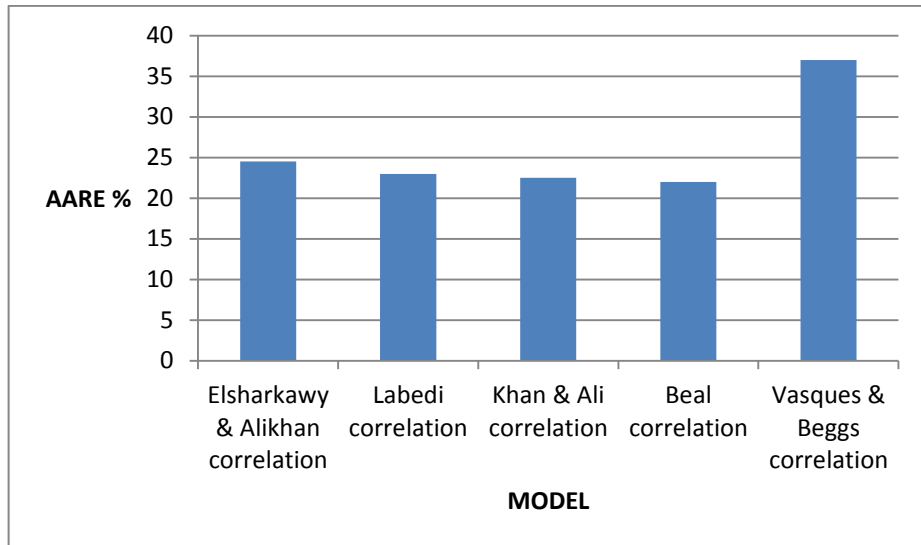
Fig(4) average relative error and absolute average relative error of undersaturation oil for every model

Conclusion

Most common method for calculating viscosity of crude oil is the viscosity correlations.

In this work the following conclusion have been obtained during the investigation

➢ Bergman and Beggs & Robinson ,are the best correlations, and most accurate for Dead Oil Viscosity, due to the less error percent. It is not preferred to Naseri and Hossain correlations; because of it is high proportion of error.

➢ Modified Kartoatmodjo and Elsharkawy & Alikhan correlation are the best and accurate for saturation oil viscosities, also it is not for favor to use Labedi, and the Kartoatmodjo & Schmidt correlation.

➢ Beal's and Khan & Ali correlation are preferred to get accurate results for of the Undersaturated oil, and it is not recommended to apply

Kartoatmodjo & Schmidt , and Vasques & Beggs correlation due to the high proportion of error.

➢ The best estimate of the dead, saturated, and undersaturated oil viscosity for Libyan crude oil exmined in this study was found to be provided by Bergman, modified Kartoatmodjo, Beal's correlations for each type respectively.

References

[1] M. A. Mahmod , M .A .A l Marhoun, Calculation for fluid physical property prediction. Journal of Petroleum Science and Engineering 23,1996

[2] Pedersen et al ,Calculating the viscosity of hydrocarbon system with pressure, temperature and composition, "Life Science Journal 1989

[3] Beggs,H.D.,Robinson "Arab J Geosic1975

[4] Kartoatmodjo,F.,Schmidt,Z, Iranian Journal of Oil & Gas Vol.3(1994)

[5] BEAL,C,.Trans,AIME Handbook of physical properties of rocks and minerals,1964

[6] Elsharkawy,A.M,Nikahan,A,A, , Trans.AIME, vol.146,pp,54-62,1999

[7] Naseri, A.,Nikazar,M.,Mousavi, Anumarical technique for an accurate determination of formation resistivity using FR – RO Overlays method "Arab J Geosic(2015)

[8] Petrosky,G.E,Farshad,production operations symposium Energy Sources ,1July 2001, vol.23,n06,pp.589-596.

[9] Egbogah,E.O.,Ng,1997, Petrophysics ,ISBN 0-88415-634-6

[10] Al-Marhoun MA,The Coefficient of Isothermal Compressibility of Black Oils, Paper SPE 81432 presented at the SPE Middle East Oil, (2003)

[11] HOSSAIN,M.S.: "Assessment and Development of Heavy Oil Viscosity Correlations" M.S. Thesis, The University of Tulsa, Tulsa, OK, 2005.

Investigation of Physicochemical Analysis Of Water Sources In Al- Jabal Al-Gharbi region, Libya

Abdulbasit M. Abeish

Chemistry Department-Faculty of Science/Assabaa- Gharyan University, Libya

[*]Corresponding author: abeesh_200875@yahoo.com

الملخص

مصادر المياه في منطقة الجبل الغربي محدودة للغاية وتحتاج إلى اجراء الدراسات اللازمة لمعرفة إمكانية استخدامها إما كمياه شرب أو في الأنشطة البشرية الأخرى. لذلك تم دراسة العديد من المعايير الفيزيائية والكيميائية لمصادر المياه في منطقة الجبل الغربي الواقعة شمال غرب ليبيا. تمت الدراسة على ثلاثة مصادر للمياه غير المعالجة وهي الآبار الجوفية ومياه الأمطار ومياه النهر الصناعي. أما بالنسبة لمياه الشرب تم فحص المياه التجارية المعالجة سواء المعبأة أو غير المعبأة. الخواص التي تم فحصها هي الأس الهيدروجيني pH ، التوصيلية ، الملوحة ، العكارة ، المواد الصلبة الذائبة الكلية TDS ، الكلور ، النترات (NO3) ، النتريت ، الكبريتات ،الفوسفات ، الحديد و النحاس. أظهرت النتائج المتحصلة عليها أن المياه الجوفية ومياه النهر الصناعي تحتوي على تراكيز عالية من المواد الصلبة الذائبة TDS تراوحت ما بين 1115 و 4090 ملجم / لتر مما أدى إلى زيادة العسر الكلي TH في هذه العينات. بينما احتوت معظم عينات المياه المعالجة على تراكيز منخفضة جدًا من المواد الصلبة الذائبة مما قد يسبب فقدان الأملاح المعدنية المفيدة للمستهلكين. من جهة أخرى ، فإن عينات مياه الأمطار احتوت على القيم المثلى للمواد الصلبة الذائبة بالإضافة إلى المعلمات الأخرى. أما فيما يتعلق بتركيز النترات NO_3 ، كانت جميع العينات ضمن الحدود المسموح بها وتراوحت من 0.02 إلى 15 ملغم / لتر. علاوة على ذلك ، كانت جميع الأيونات الكيميائية التي تم فحصها في هذا البحث مثل الحديد والنحاس ضمن إرشادات منظمة الصحة العالمية.

ABSTRACT

Water sources in Al-Jabal Al-Gharbi area are very limited and need to be studied for use either as drinking water or human activities. Therefore, several physical and chemical parameters of water sources in Al-Jabal Al-Gharbi region located in Northwest of Libya were investigated. For untreated water three sources were studied including groundwater wells, rain water, and Man-Made River (MMR). However, for drinking water packed and unpacked treated commercial water were investigated. The examined properties were pH, conductivity, salinity, turbidity, total dissolved solids (TDS), chlorine, nitrates (NO^-_3), nitrites, sulfate, phosphate, iron, and cupper. The results showed that the groundwater and MMR water had high TDS concentrations between 1115 and 4090 mg/L leading to increase the total hardness in these samples. Most of the treated waters had very low of TDS concentrations causing loss the useful salts for consumers . However, the rain water samples had optimum values of TDS and other parameters. Regarding NO^-_3 all samples were within the limitation and in the range of 0.02 to 15 mg/L. Furthermore, all metal ions examined in this work such as iron and Cupper were within the WHO guidelines.

Key Words: Physicochemical properties, Water quality, Water Sources, Libya

1.Introduction

Water pollution has become one of the main threats that face humanity today. Increasing everyday people activities lead to contamination of water sources including oceans, rivers, lakes and groundwater. This contamination contributes to generating large amounts of polluted water that people cannot use in their daily life. Contaminated water is generated from many different sources involving petroleum refineries, dyes, drugs, paper, textile dye, detergents, surfactants, pesticides, herbicides, insecticides and pharmaceutical manufacturers [1]. These chemical contaminants can be organic pollutants such as alkanes, aliphatic, alcohols and aromatic compounds or inorganic like heavy metals, including lead, mercury, nickel, silver and cadmium. In addition, water can be contaminated by pathogens such as bacteria, viruses and fungi [2]. The negative impact of different polluted components on the environment, human health and aquatic live is extremely significant [3].

Released waters without monitoring their specifications can be absorbed by soil layers leading to contaminate surfaces and groundwater [4]. Some of organic hazardous substances can be decomposed during the time, however; most of them remain for longer time. According to that the most of the groundwater generates from rain and snow so these biorefractory pollutants can be precipitated with this water and entered the earth layers [5]. Heavy metals can be generated from many different ways such as natural sources, mining, and industrial activities [6]. These toxic pollutants like Hg, Pb, and Cd are categorized as carcinogen compounds causing various dangerous diseases [7]. Libya is one of the semi-arid countries due to the low rainfall and limited amounts of groundwater. Water resources in Libya can be categorized to two types including conventional water resources (surface and groundwater) which represents about 97.3% and non-conventional water resources (seawater desalination and treated water) that represents about 2.7% [8]. Hence, the life in this country especially Al Jabal Al Gharbi area totally depends on the groundwater that is treated to use it as drinking water. However, there is also two other sources originally coming from out of the study area which are rainwater and Artificial Al Naher water. For rain water there is no significant amounts can be collected except that from roofs of some houses and people use it as drinking water. However, for Artificial Al Naher water can be considered as an important source due to the large amount of water that can be obtained from it, but people in this area do not use it as drinking water. Water purification stations are rapidly growing as a source of drinking water in the world [9]. In general, for drinking water people in the study region use packed and unpacked treated water that mainly come from groundwater. The treatments are performed to reduce the salts and hardness to give the water acceptable taste. However, the water comes from purification stations can be contaminated ether chemically or biologically. All these sources should be investigated to see the degree of pollution and to what extent they follow the standard specifications of the quality water. Therefore, the aim of this study is to investigate the physical and chemical quality of all water sources in Al Jabal Al Gharbi region and keep track of any potential contamination sources. Furthermore, it focuses on how much treated water fulfills the WHO guidelines for drinking water.

2. Materials and Methods

2.1 Samples Collection

Seventeen samples were collected from different water sources located in Al Jabal Al Gharbi district in Jul, 2020. The study area as shown in (Fig. 1) located Northwest in Libya and coordinates 31°45'0.00" N 12°30'0.00" E.

Figure 1 Al Jabal Al Gharbi District Location

These samples were Four groundwater samples, six packed treated water, four unpacked treated water, one sample of rainwater, and one sample of Man-Made River (MMR) water. All fresh samples were obtained directly from the head of the wells for groundwater and from the taps for unpacked treated water. The samples were stored at $4C^0$ to avoid any type of degradation and the investigations were carried out in the laboratory immediately next day of work.

2.2 Materials and Equipment

All experiments were conducted using distillated water. chemicals used in these experiments were checked for expire dates. Sodium hydroxide (NaOH 0.02N) and sulphuric acid (H_2SO_4 0.02N) were prepared and used. EDTA (0.8N). Potassium chromate, Phenol Phthelene and Methyl Orange Indicators.

2.3 Laboratory Procedures

The physical and chemical investigations of the samples were performed according to different laboratory methods. Various quality parameters were

effectively investigated including Colour, smell, taste, pH, conductivity (Ec), salinity (Sal.), turbidity (NTU), total dissolved solids (TDS), chloride (Cl^-), nitrates (NO_3^-), nitrites (NO_2^-), sulfate (SO_4^{-2}), phosphate (PO_4^{-3}), iron (Fe^{-2}), and cupper (Cu^{+2}). Spectrophotometer HACH DR/2010 was used to detect most of the variables

3. Results and Discussion

Seventeen water samples were analyzed in order to determine the physical and chemical parameters. All results achieved were validated using WHO standards. Table 1-3 shows the obtained results of untreated water samples including five groundwater wells, MMR water and the rainwater.

Table 1 Untreated Water Analysis

Water Source	Location	pH	Ec ms/cm	Sal	Turb NTU	TDS mg/L	SO_4^{-2} mg/L	NO_3^- mg/L	NO_2^- mg/L	Cl^- mg/L	PO_4^{-3} mg/L	Fe^{+2} mg/L	Cu^{+2} mg/L
Well 1	Gharian	9.0	1541	0.04	7	**1115**	400	15	0.1	0.4	0.06	0.04	0.01
Well 2	Gharian	8.2	1230	0.03	5	**1070**	365	8	0.09	0.2	0.05	0.07	0.02
Well 3	Assabaa	8.0	1123	0.04	4	**1000**	321	5	0.1	0.3	0.07	0.03	0.01
Well 4	Arabta	8.1	2994	1.8	6	**1488**	600	16.3	4.3	0.06	0.06	0.21	0.09
Well 5	Mizda	9.1	6000	8.6	7.5	**4090**	1400	6	0.1	0.05	1.71	0.02	2.37
MMR	Assabaa	8.2	2750	1.2	5	**1248**	415	17	6	0.3	0.37	0.02	0.52
Rain	Gharian	7.4	286	o.1	3	134	16	5.6	.001	1.08	0.004	0.04	0.01

It can be noticed that most of the samples except rainwater have a bit high of pH between 8.0 and 9.0 which might be due to the presented salts in these samples. This fact can be supported by the high concentrations of TDS leading to unacceptable taste and scale formations in the pipes. These salts include SO_4^{-2}, CO_3^{-2} and HCO_3 in terms of magnesium and calcium. However, the other parameters involving NO_3^-, NO_2^-, Cl, PO_4^{-3}, Fe^{+2} and Cu^{+2} were within the limitations. Figures 2 and 3 illustrate the most important factors in this study which are TDS and NO_3^- concentrations of all samples and compare them with standard values.
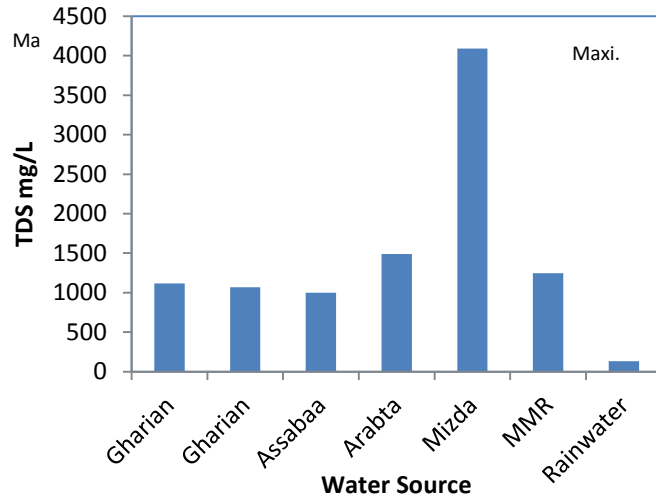
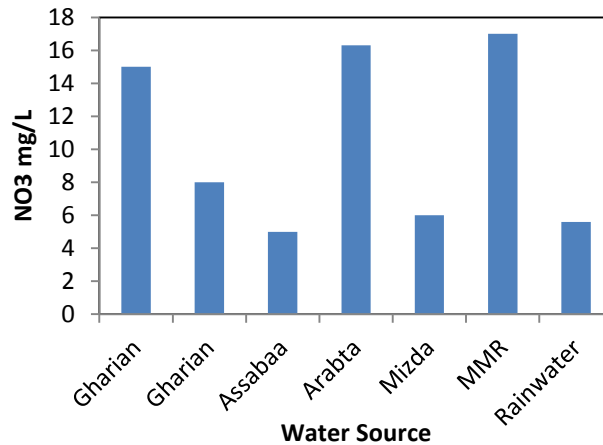**Figure 2 TDS Concentrations of various untreated water**

Figure 3 NO⁻₃ Concentration of various untreated water

Table 2 gives results of the same parameters for unpacked treated water. It can be seen that all factors within the standard ranges and some of them below the minimum values. For instance, the sample of station 2 has just 99 mg/L of TDS which means that there is no enough salts. This result can lead to extract all beneficial compounds from water and becomes unhealthy. However, most people in the study area consume this type of water. Figure 4 shows the TDS concentrations of four unpacked treated water samples and compares the result with the maximum acceptable value.

Table 2 Unpacked Treated Water Analysis

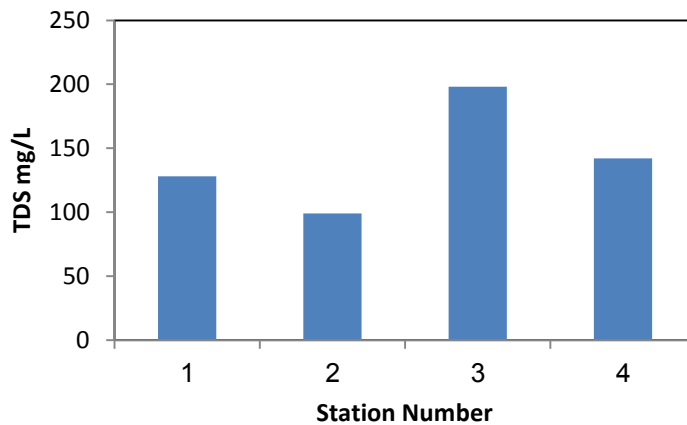| Station NO.	Location	pH	Ec ms/cm	Sal	Turb NTU	TDS mg/L	SO_4^{-2} mg/L	NO_3^- mg/L	NO_2^- mg/L	Cl^- mg/L	PO_4^{-3} mg/L	Fe^{+2} mg/L	Cu^{+2} mg/L
1	Gharian	8.5	220	0.03	3.8	128	18	3	0.04	0.05	0.08	0.06	0.01
2	Gharian	8.2	112	0.09	1.5	99	12	1	0.001	0.07	0.08	0.05	0.06
3	Gharian	7.6	221	0.09	3.6	198	14	0.06	0.001	0.02	0.02	0.16	0.08
4	Assabaa	8.2	144	0.03	3	142	12	0.05	0.03	0.04	0.03	0.13	0.04

Figure 4 TDS Concentrations of various unpacked treated water

Table 3 shows the obtained results of packed treated water samples of different commercial brands. Even though there is no a big difference compared to unpacked water but TDS concentrations still very low especially Al Safia and Al Jazeera brands. However, this type of drinking water can be considered as more safe than unpacked one due to safe packing processes. In other word, in an unpacked treated water sector all people deal in a direct way to fill their bottles leading to a possibility of biological pollution.

Table 3 Packed Treated Water Analysis

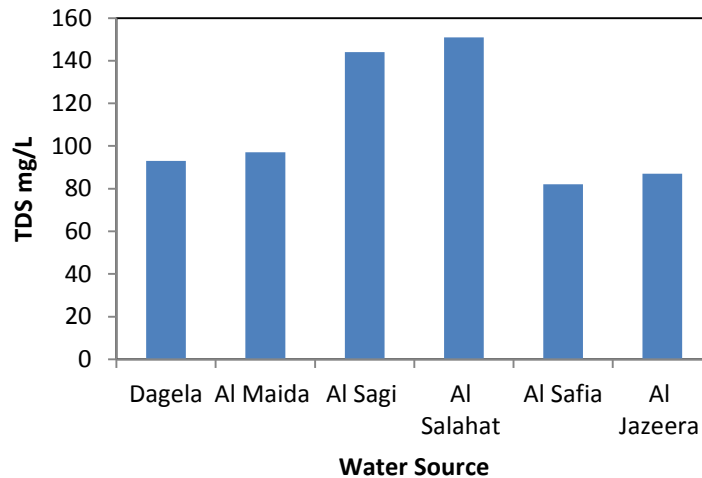| Water Brand	pH	Ec ms/cm	Sal	Turb NTU	TDS mg/L	SO_4^{-2} mg/L	NO_3^- mg/L	NO_2^- mg/L	Cl^- mg/L	PO_4^{-3} mg/L	Fe^{+2} mg/L	Cu^{+2} mg/L
Dagela	8.2	98.1	0.05	1.8	93	7	0.06	0.001	0.07	0.01	0.17	0.07
Maida	7.4	105	0.01	2	97	6	0.4	0.02	0.2	0.07	0.12	0.01
Sagi	8.4	146	0.07	1.9	144	17	0.04	0.01	0.19	0.04	0.03	0.02
Salahat	8.9	156	0.01	2.3	151	16	0.02	0.01	0.22	15	0.08	0.05
Safia	8.3	96	0.01	2.4	82	12	0.06	0.01	0.11	0.05	0.11	0.01
Jazeera	7.6	183	0.01	2.2	87	18	0.08	0.02	0.13	0.03	0.04	0.03

Figure 5 TDS Concentrations of various packed treated water

Figure 5 illustrates the TDS results of six packed treated water samples and compares the results with the maximum acceptable value.

4. Conclusion

In conclusion, the TDS concentrations of all groundwater and MMR water samples were very high especially the sample of Mizda city. This high

parameter gives the water unacceptable taste and raises the total hardness causing scales in water equipment and ineffective washing. However, the all other properties particular NO_3^- were within the limitations of standard water quality. The packed and unpacked treated water samples had good quality due to the reduction of TDS using commercial treatment systems. However, it can be noticed that some of these kinds of drinking water have very low TDS meaning lack of useful chemical elements. This can cause reduction of these beneficial elements in the human bodies and lead to poor blood diseases. The rainwater was the optimum value for all parameters and had very high quality of drinking water. To increase and enhance the water sources more water treatment stations should be implemented.

References

[1] Chong, Meng Nan, Bo Jin, Christopher WK Chow, and Chris Saint. 2010. "Recent developments in photocatalytic water treatment technology: a review." *Water research* no. 44 (10):2997-3027.

[2] Gogate, Parag R, and Aniruddha B Pandit. 2004. "A review of imperative technologies for wastewater treatment I: oxidation technologies at ambient conditions." *Advances in Environmental Research* no. 8 (3):501-551.

[3] Smołka-Danielowska S., 2006. Heavy Metals in Fly Ash from a Coal-Fired Power Station in Poland. University of Silesia, Faculty of Earth Sciences, ul. Będzińska 60, 41–200 Sosnowiec, Poland. Polish J. of Environ. Stud., 15(6), 943–946.

[4] Demaku S., Shehu I., Jusufi S., Arbneshi T., Dobra B., 2011. Heavy Metals in Coal Ash, Soil, Water and Sludge near the Two Coal-Fired Power Stations in Kosovo. J. Int. Environmental Application & Science, Vol. 6, 412–416.

[5] Jaguś A., Skrzypiec M., 2019. Toxic Elements in Mountain Soils (Little Beskids, Polish Carpathians). Journal of Ecological Engineering, 20(1), 197–202.

[6] Chen J.P, Wang L.K, Wang M.H.S, Hung Y.T, Shammas N.K., 2017. Remediation of heavy metals in the environment. CRC Press Taylor & Francis Group 6000 Broken Sound Parkway NW, Suite 300 Boca Raton, FL 33487–2742.

[7] Fulekar M.H, Dave J.M., 2007. Release and behavior of Cr, Mn, Ni and Pb in a fly ash/soil/water environment: column experiment. International Journal of Environmental Studies, 38(4), 281–296.

[8] Brika, B. 2019 "The water crises in Libya: causes, consequences and potential solutions. Desalination and Water Treatment, 351-358.

[9] Amy. G., Ghaffour, N., Li, Z, Francis, Li., Linares, R. V., Missimer, T., & Lattemann, S. 2017 "Membrane-based seawater desalination present and future prospects" Desalination, 401, 16-21.

The Effects of Land Use Changes in Malaysia on the Structural Characteristics of Soil Organic Matter.

Fathia Alaswad[1], Hakim shebaani[2], Mohamed M. Alghiryani[3],Melod M. Unis[4].

1,2,3,4- Higher Institute of Sciences And Technology, Gharyan. Libya.

الملخص:

تم دراسة تأثير استخدام الأراضي على تغير محتويات الكربون والخصائص التركيبية للمادة العضوية في التربة، حيث تم استخدام التحليل الطيفي للأشعة تحت الحمراء وتم فحص عينات التربة من مزارع مختلفة مثل مزارع المطاط ، ومزارع زيت النخيل بأعمار مختلفة 5 و 15 عام ، بالإضافة إلى مراعي الثمام الكبير وذلك في النطاق الرئيسي لشبه جزيرة ماليزيا، وذلك لغرض تحديد آثار تغير استخدام الأراضي على محتويات التربة من الكربون العضوي والخصائص التركيبية للمادة العضوية، ومن ثم تمت دراسة التحليلات الكيميائية والخصائص التركيبية لعينات التربة حتى عمق 30 سم.

وقد أظهرت أطياف الأشعة تحت الحمراء للآفاق العضوية السطحية زيادة في النطاق الأليفاتي (2920 سم -1) مع زيادة في النيتروجين الناتج عن الحفظ الانتقائي للتركيبات الأليفاتية المشتقة من النباتات الأصلية ذات المحتوى العالي من الشمع (المطاط) بالاضافة لإستخدام الأسمدة.

توضح هذه الدراسة أن الاختلافات في محتويات الكربون مرتبطة بالاختلاف المشترك للغطاء النباتي، ومع ذلك فإن الغطاء النباتي هو المحرك الرئيسي للاختلافات في الخصائص التركيبية للمادة العضوية.

Abstract:

To investigate the effect of land use change carbon (C) contents and structural characteristics of organic matter (OM) in soils. Fourier-transform infrared (FTIR) spectroscopy was used. Soil samples from different plantation rubber (Hevea brasiliensis), oil palm (Elaeis guineensis) with different age 5and15 years old, and pasture (Pancium Maximum)) in the Main Range of Peninsular Malaysia were investigated to determine the effects of land use change on soil organic carbon (SOC) contents and structural characteristics of OM. Chemical analyses and structural characteristics of soil samples from 0 to 30 cm were analyzed. FTIR spectra for the surface organic horizons showed an increase of aliphatic band (2920 cm^{-1}) with increasing nitrogen, that resulted from a selective preservation of aliphatic structures derived from original plants with high content of waxes (rubber) and using fertilizer. This study demonstrates that differences in (C) contents is related to co-variation of vegetation; however, vegetation is the major driver of differences in structural characteristics of OM.

Key words: land use change, soil organic carbon, structural characteristics of soil organic matter, FTIR.

Introduction:

It is known that soil organic matter, especially soil organic carbon , plays an important role in repairing and improving many soil properties. Agricultural land is the land most closely associated with the main functions and optimal level of soil organic carbon. Forestry and grazing, in addition to groundwater contamination and carbon sequestration, are areas closely related to the function of soil organic carbon (SOC). A key component of the global carbon cycle are the emissions from land use and land cover change (Gasser et al.,2020), generating around $1.5 \pm 0.7 PgCyr^{-1}$ of the total carbon dioxide (CO_2) emissions around the world (Friedlingstein et al., 2019), and causes to declines in soil organic matter (SOM) that represents the largest terrestrial pool of carbon (C) in the world (Zhu et al., 2016). Land use and land cover change are known to strongly impact the chemical composition of SOC. The changes in the chemical composition of SOC it will strongly effects on the decomposition rate of SOC, which in turn effects on SOC stabilization and global carbon cycle. In Malaysia, human activities, such as land-use change and tree cutting, have significantly altered the natural forests that strongly influence the chemical composition of (SOM). Since the spare of information on the effects of land use change on the structural composition of SOM and, as Fourier transform infrared spectroscopy (FTIR) has served as a valuable tool to characterize qualitatively of chemical groups of which SOM is comprised, therefor it was used in this study to investigate the effects of land use change on SOM composition.

Materials and Methods: Study Area:

This study was conducted in agricultural plantation of rubber plantation (Hevea brasiliensis) that is 15 years old as well as two different aged oil palm plantation (Elaeis guineensis) five and fifteen years old respectively, and Pasture (Pancium Maximum) at the University Putra Malaysia (UPM) farm, Serdang, Selangor, Malaysia, as demonstrated in Figure1. The soil classified as Serdang at UPM. An experimental plot of (100 × 100 m) with three replicates was designed for the field experiment.
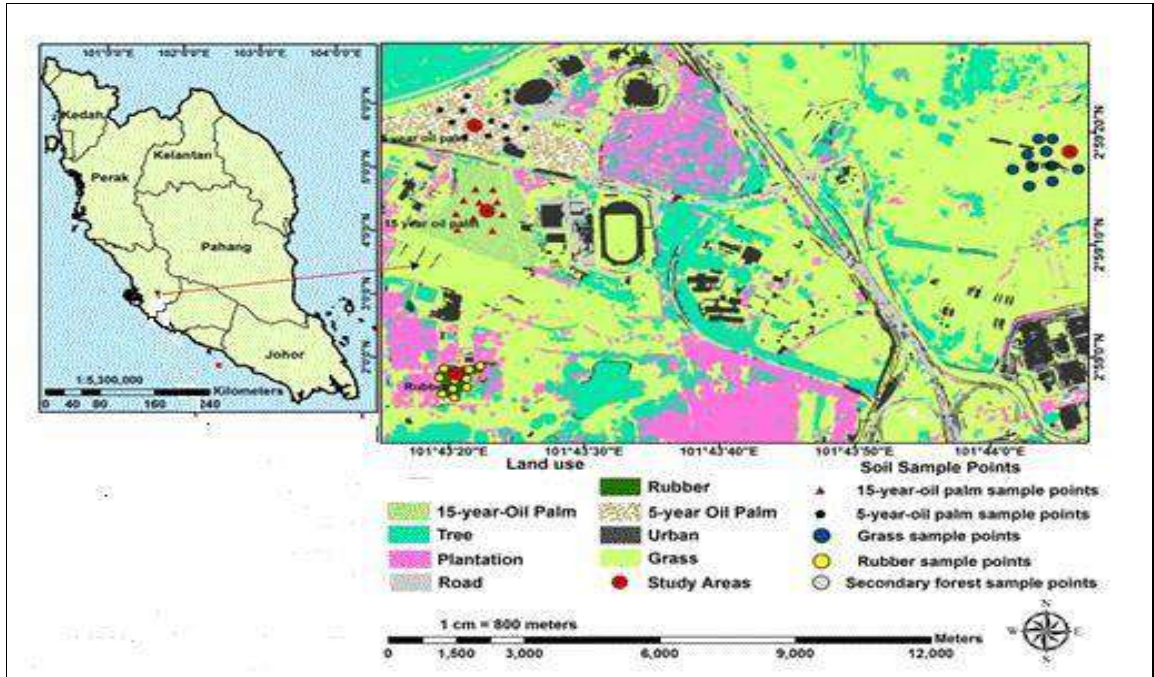
**Figure 1: The study area in the University Putra Malaysia (UPM) farm.
Selangor State, Malaysia.**

The geographic coordinate were shows in Table 1 as determined by Global Positioning System (GPS) Garmin 60CSX.

Soil sampling:

Soils were sampled using steel rings soil sampler, the depth intervals sampled was (0– 30cm),samples were collected from 3 replicate for each sites.

Table 1: General description of the study sites.

Site profile/ Plant information	Geographic coordinate in the study area		Geological information	Family	Soil texture
	Latitude (N)	Longitude (E)	(Jusop et al., 1979)		
1/Rubber plantations	02 58 58.4	101 43 20.2	Typic Paleudlt	isohyperthermic, Typic Paleudlt	Sandy clay loam
2/15 years oil palm	02 59 11.0	101 43 24.6	Tropeptic Haplorthox	Fine loamy, kaolinitic, isohyperthermic	clay
3/5 years Oil palm	02 59 21.7	101 43 23.4	Typic Paleudult.	Clayey, kaolinitic, oxidic isohyperthermic	clay
4/ Pasture	02 59 27.4	101 43 59.3	Tropeptic Haplorthox	Fine loamy, kaolinitic, isohyperthermic	clay

Soil analysis:

Bulk soil samples from all genetic horizons were homogenized, air-dried, gently ground, and passed through 2 mm sieve prior to the physical and chemical analyses. Soil pH was measured using a glass electrode in a supernatant suspension of 1:2.5 soil/water and KCl ratio.OM was analyzed by loss on ignition method according (Heiri et al., 2001), total carbon and nitrogen according to (Zulkifli et al., 2014). For SOM decomposition soil samples were finely ground (<65 μm) and heated at 60 °C for 48 hours to reduce the influence of water content on interpretation of the spectra. FTIR Spectroscopy was used and performed with a Perkin Elmer Spectrum 100 spectrometer (Jafarzadeh-Haghighi et al., 2015). However, (Table 2) shows the main IR absorption bands and their corresponding assignments for the samples of soil.

Statistical analysis:

Regarding the effect of land use change on soil chemical and geo-physical properties, a two way MANOVA was used to analyses the data, with Tukeys post-hoc tests to separate the means.

Table 2: The main IR absorption bands and their corresponding assignments for the samples of soil.

Band(cm^{-1})	Base points for the integrated bands (cm^{-1})	Assignment
3693		Stretching of OH groups (bonded and non-bonded (Wang et al., 2016).
3620		Hydroxyl groups (water molecules alcohols, phenols), (Rumpel et al., 2002).
3446	3700-3200	(Si-O±H vibrations), (Tatzber et al., 2011).
3373		Stretching vibration of hydroxyl bonded and non-bonded groups,(Santana et al., 2013).
2920	2800-3000	Symmetric and asymmetric stretching vibrations, respectively of (aliphatic C-H bonds in methyl and/or methylene b - CH3, CH2, and CH groups of alkyls), (Rumpel et al., 2002; Tatzber et al., 2011).
1778	1700-1790	C=O stretching vibration of carboxyl groups, aldehyde and ketones, (Tatzber et al., 2011(Wang et al., 2016).
1639-1625	1570-1700	C=O stretching vibration of carboxylates and Amides, aromatic C=C stretching vibration aromatic C=C bonds conjugated with C=O bonds of unsaturated ketones or amides, (Santana et al., 2013; Wang et al., 2016).
1398	1330-1400	C–O stretching vibration of C-H bending vibration e, phenolic OH D, CO-CH$_3$, COO- antisymmetric stretching vibration, (Duboc et al., 2012).
1249	1000-14000	CH and NH (amide II) bending motions, molecule skeletal vibrations and aromatic stretch, to carbon oxygen bond vibrations, (Duboc et al., 2012). C–O stretching vibration of aryl ethers and phenols, (Haberhauer & Gerzabek, (1999).C-O stretching vibration and O-H bending vibration of COOH, (MacCarthy & Rice, 1985).

| 1112 | 950-1170 | C-O stretching vibration of polysaccharides, Si−O stretching band, (Santana et al., 2013).FC-O vibration of ether groups, (Rumpel et al., 2002). |
| 910-750-690528-414 | 910, 790, 690, and 540 | Bands of inorganic materials, such as quartz minerals and clay, (Tatzber et al. 2011). |

Nonetheless, in order to get a clear understanding of the impact of land cover change on the composition of SOM, and to compare differences in the constituents of functional group to the quality of SOM, it's necessary to calculate two band ratios. The two indices employed ratios of bands which are representing functional group types (i.e., aliphatic, O-functional group). In previous studies these were established as indexes of comparative decomposition and resistance or recalcitrance of SOM .

$$\text{Index I} = \frac{\text{aromatic}}{\text{aliphatic}} \dots [1]$$

$$\text{Index II} = \frac{\text{C function group}}{\text{O function group}} \dots [2].$$

Index I was postulated or hypothesized to be a metric for decomposition which was taken as the ratio of aromatic to aliphatic functional groups, while ratios of bands that are representing the two functional groups are shown to rise up with increasing degree of decomposition (Margenot et al., 2017). Index II was hypothesized as a ratio of C- to O-functional groups: an increase or the rise of which is associated with higher recalcitrance or resistance of SOM (Margenot et al, 2015).

Results and Discussions:

The chemical properties of PH, TOC, and OM of rubber (R), 15 years oil palm (15Op), 5 years (5Op)oil palm and pasture (P) were studied.

Tables 3 summaries the chemical characteristics of soils under investigation:

Plantation site	pH	TOC	TON
R	4.42±0.4	1±0±0.2	0.08±0.02
OP 15	4.68±0.41	1.34±0.5	0.11±0.05

| **OP 5** | 4.36±0.76 | 1±0.2 | 0.89±0.02 |
| P | 4.39±0.53 | 1.83±0.9 | 1.76±0.1 |

Soil pH :

The analysis showed that, the pH value of all sample was between 4. 36 to 4.68. In general, pH of the Ultisols and Oxisols in Malaysia have low pH values in the range of 4 to 5 would attributed to the high rainfall (≥2000mm), the nature of parent material and the hydrolysis of aluminum as suggestion by (Fatai et al., 2017).

TOC:

The results of the effect of TOC under the land use clarify that, the highest TOC content found in pasture, oil palm 15years, oil palm 5 years and rubber consequently can be attributed to the diverse type of vegetation that produces much litter through the fallen leaves, stem, and branches of trees and plants.

Studies have also demonstrated that the higher TOC under oil palm plantation was due to the decomposition of added plant materials such as the application of empty fruit bunches and fibrous root system . However, higher the below-ground production of photosynthetic and fungal hyphae are probably responsible for the high amount of total organic matter in pasture (Chemeda et al., 2018).

TON:

As seen in Table 3 , the pasture site had significantly greater TON content than the top soil of 15 and 5 years oil palm as well as that in the rubber plantation. In our study, we found that land use type had significant effect on TON distribution. This is because soils with different vegetation cover have different litter decomposition processes which leads to differences in the release of C and N in the soil. Previous investigators (Deng et al., 2016) had reported that tree species with different plant traits and stand properties can impact on retentions of soil organic C and N, for instance on releasing nutrients to soil via mineralization. The pasture and oil palm 15 years had higher TON than rubber plantation, which is likely due to the input of organic matter derived from roots in pasture, and from roots and frond heap in oil palm plantations that compromise higher quantity of nitrogen compounds

such as protein and amino acids. Similar results were obtained by(Haron et al. 1998), in Malaysia and by (Frazão et al. 2013) in Brazil.

Meanwhile the 15-year-old oil palm had higher soil N than the oil palm for 5 years, the authors suggest that by increasing the planting age of the oil palm, the amount of C and N storage increased after the change of land use in the soil. These results are in line with (Roslee et al., 2016) who indicated that oil palm sequestered C and N during growth. Furthermore, increasing the pH value under plantation might have increased the OM decomposition in the soil, and hence promote the mineralization processes .

SOM compositions:

Evaluated of soil sample from R, P, OP15, and OP5 were documented by FTIR spectroscopy. The data in Figure 2,3,4 and 5 shows the IR absorption band and related function group of SOM in each site. The resulting infrared spectra of soils from R, P, OP15, and OP5 were found to be similar in their elementary peak assignments, as shown in Figure 2,3,4 and 5.
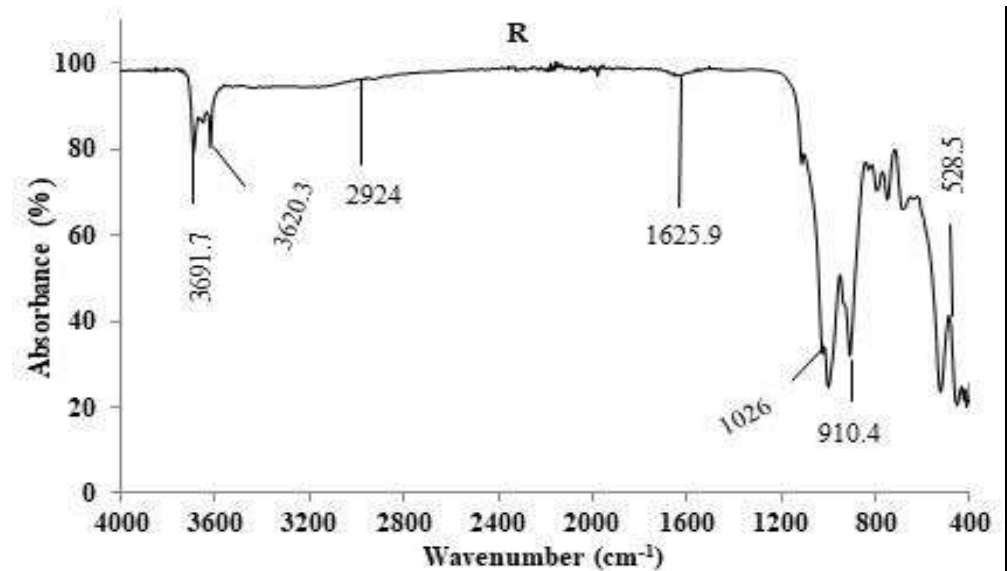

Figure 2: FTIR sample spectra of topsoil from chosen sites (R: rubber plantations). Spectra have been stacked by Y offsets.
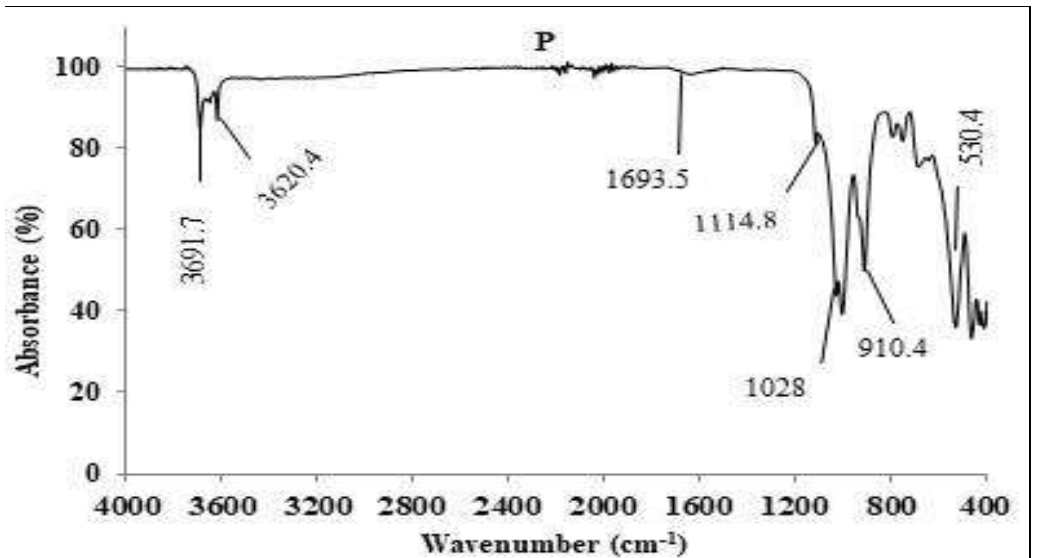
Figure 3: FTIR sample spectra of topsoil from chosen sites (P: pasture). Spectra have been stacked by Y offsets.
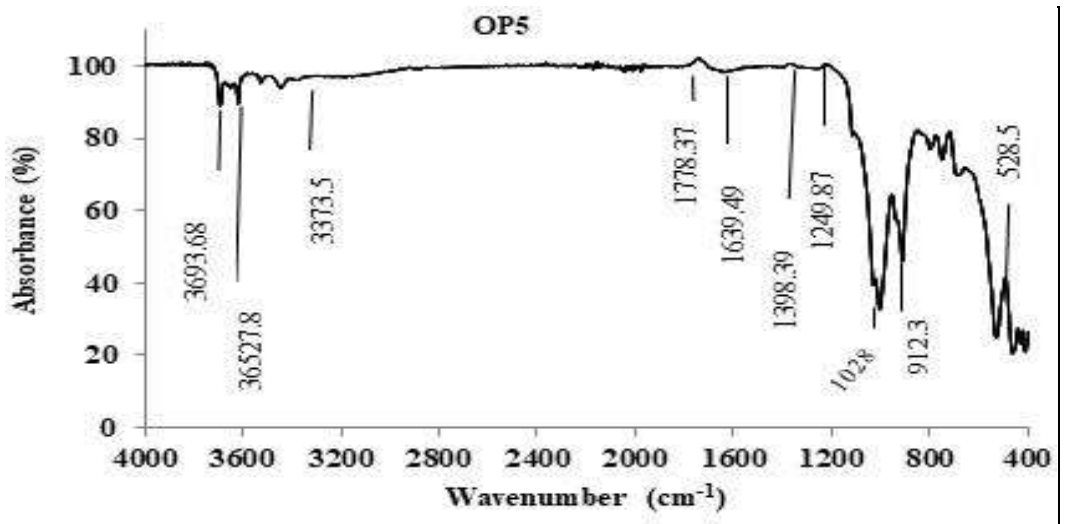

Figure 4: FTIR sample spectra of topsoil from chosen sites (OP5: 5 years old oil palm plantations). Spectra have been stacked by Y offsets.
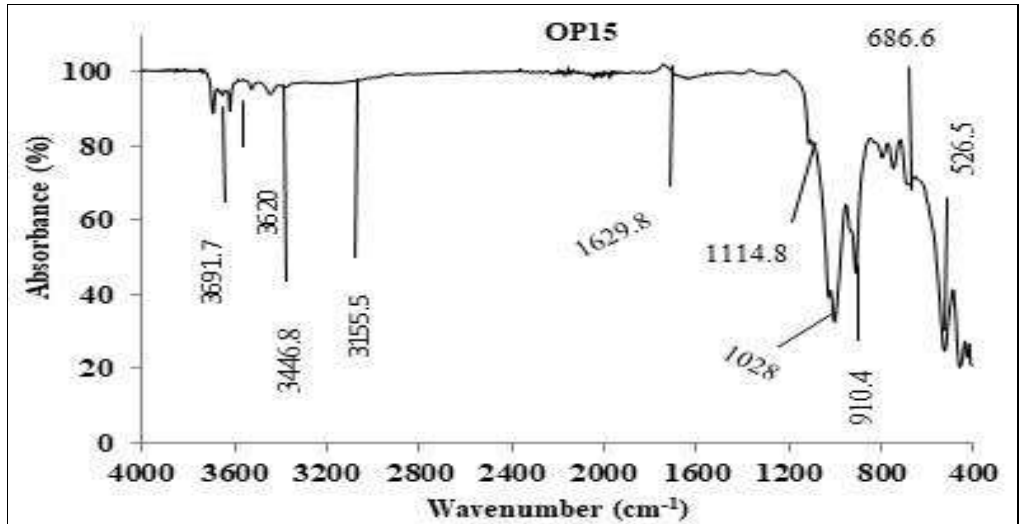
Figure 5: FTIR sample spectra of topsoil from chosen sites (OP 15: 15 year old oil palm plantations). Spectra have been stacked by Y offsets.

Findings in Figure 2,3,4and 5 indicate the peak patterns of the soils spectra at the 4 sites were comparable. The aliphatic group (either C-H stretching vibrations at 2920 cm^{-1} was appeared in R. While, the carboxyl group (C=O) stretching vibration at 1778 cm^{-1} was observed only in OP5. Meanwhile, aromatic (stretch H band at 3693-1630 cm-1), amides and carboxylates groups (C=O) stretching vibration at 1639-1625 cm^{-1}), CH and NH (amide II) bending motions, and aromatic stretch vibration at 1000-1398 cm^{-1} were observed at all study sites. Interestingly, with the presence of peak at 3620 cm^{-1}, which was assigned to hydroxyl group (O–H), stretching vibrations of minerals, indicating existence of kaolinite clay and montmorillonite in the study sites as suggested by (Nguyen et al., 1991). This shows the main mineral constituent in the top soil of study sites are S + C fractions, and it is expected that the small integrated areas for the CH- region came to be as a result of the hydrophobic moderation of aliphatic chains and surfaces of mineral as suggested by (Djomgoue and Njopwouo 2013). The moderation or interaction between mineral surfaces and aliphatic chains have been identified as very important in the materialization of soil aggregates and the stabilization of and gano-mineral complexes (Kleber et al., 2007).

Other bands positioned in the fingerprint area (414-1000 cm^{-1}) at (R, P, OP15 and OP5) sites, were accordingly assigned to couple vibrations. Bands

in this type of region indicated the complexity of the studied and analyzed samples as and Jafarzadeh-Haghighi et al., (2015) observed. Top soil indicated higher number of absorption bands, particularly in the fingerprint area as matched to other absorbance band. The range of bands between 1000 and 1026 cm^{-1}, which showed evidence of the presence of polysaccharides in the topsoil, could similarly be assigned to Si-O vibration of minerals in the sample of soil. This observation happens to be in an agreement with the results of humus and mineral layers highlighted by Jafarzadeh-Haghighi et al. (2015), and similar association was noticed by Tatzber et al., (2011). The peak around 600-400 cm^{-1} was linked with unidentified mineral compounds (e.g., oxides, silicate, ond organo-mineral fractions) (Wang et al., 2016).

More pronounced in the sample soil of R is the aliphatic bands. The presence of aliphatic bands and the concentration of aliphatic stretching vibration (band 2920 cm^{-1}) may be linked to the rise in the plant materials decomposition and the process of humification as augmented by the higher index value (I) as shown in Table 4.

Table 4: The index value of SOM rubber (R), pasture (P), 15 years old oil palm (OP15) and 5years old oil palm plantation (OP5).

Land use	Index I = (aromatic/aliphatic)	Index II = (C function group/O function group)
R	1.436	1.93
P	1.625	2.12
OP5	2.974	2.41
OP15	2.005	2.58

Related trend was also detected by Rumpel et al., (2002) for Cambisol and Podzol under spruce and beech forest of Northern Bavaria, Germany by means of ^{13}C NMR spectroscopy. In the same vein, Jafarzadeh-Haghighi et al., (2015) submitted that, the decomposition of residues of plant is predominantly linked with the fall in polysaccharides and or the related accumulation of aliphatic structures.

Nonetheless, the aromatic bands (3690-3373 cm^{-1}) at P and OP15 sites were found to be a good proof on the rising of the resistant or recalcitrant

material at the sites, as depicted by the higher value of index II (Table 4), and consequent support for the higher value of SOC at the P and OP15 sites (Table 3). Further, maximum relative proportion of aromatic C showed that organic matter that are mineral-associated and organic matter trapped at sites unreachable to microbial attack, or that are protected physically in soil aggregates, belong to an additionally stable organic matter pools with decades to centuries as a turnover time. Additionally, the lower content of aromatic within soils at R sit and the inverse higher content of aliphatic compounds are likely to be explained by the domination of sand particles (Pisani et al. 2014) corroborated that, long chain-free aliphatic lipids increase as the soil sand content increases.. Furthermore, the pH value at R (Table 3), supported (Pisani et al., 2014) result that, the organic matter associated with mineral in acid sandy soils was reported to be overwhelmed by aliphatic structures. In addition, (Lu etal., 2022) reported that, increased SOC in terrestrial ecosystems was closely associated with decreasd soil pH, which reduced soil C loss by limiting microbial degradation.

In addition, the higher percentage of amine group (3527, 3446 and 3373 cm^{-1}) at OP15 and OP5 sites respectively (figure 4-5), was a sign of the application of fertilizer in the area under study which Yu et al., (2015) reported, or due largely to the activity of enrichment with the microbialderived amide N (amide I and amide II). And this possibly is due to a stabilization of amine group by clay minerals as alluded to by (Helfrich et al., 2006) . The significantly higher content of clay at OP and P back this result. According to Jindaluang et al., (2013) 65–90% of total N assigned to amides was extant in the fine soil fractions (clay & silt). On the same vein, OP15 gave out stretch and broad alkel halide higher than OP5, which was a sign on the higher SOC content. At the same time this also lends support to the previous result, that SOC was raised by increasing the age of plantations of oil palm (Table 3).

Interestingly, the FTIR bands at P, offered broad alkel and amine groups, which are expected to be a valid indicator on the fertility of soil in compare with other sites.

This result in line with Lu et al., 2022 results, which demonstrated that, N-mediated soil acidification is the main   increasing SOC under elevated N input soil.

The inherent pattern of accumulation of C functional groups found along the sites that were studied appeared to be altered by changes in land use and nature of the size of particle as well. Therefore, this study infers that the pattern of the accumulation of SOM happened to be stimulated by the quality and quantity of organic matters of input and their rates of decomposition, and characteristics and nature of the size of soil particle as well.

Conclusions:

In this study, we investigated the impact of land-use change, i.e. conversion of rubber to tree plantations or cultivated fields, on soil quality (i.e., SOM, PH ,and TOC) at Serdang State. We found that , the conversion of rubber plantation to oil palm and pasture had positive impact on SOM. In conclusion, to maintain soil fertility, forest managers should avoid forest conversion to agriculture, you have to focus on conversion plantation to another type of plantation. This result supported the FTIR results that showed no difference change for the chemical composition of SOM relating to land use change and concluded that, the relative distribution of SOC, FTIR absorbance can be good indicators of the soil organic matter (SOM) quantity and quality. Moreover, this study recommend that the rubber cover changes into oil palm and pasture resulted in improved content of SOM as a result of addition of plant residue at oil palm plantation.

References:

[1] Chemeda1, M., , Kibret, K., Fite,T. (2018). Influence of Different Land Use Types and Soil Depths on Selected Soil Properties Related to Soil Fertility in Warandhab Area, Horo Guduru Wallaga Zone, Oromiya, Ethiopia. Int J Environ Sci Nat Res, 4(2). 1-12.

[2] Deng, L., Wang, G., Liu, G., & Shangguan, Z. (2016). Effects of age and land-use changes on soil carbon and nitrogen sequestrations following cropland abandonment on the Loess Plateau, China. Ecological Engineering, 90, 105-112.

[3] Djomgoue, P., & Njopwouo, D. (2013). FT-IR spectroscopy applied for surface clays characterization. Journal of Surface Engineered Materials and Advanced Technology, 3(04), 275.

[4] Duboc, O., Zehetner, F., Djukic, I., Tatzber, M., Berger, T. W., & Gerzabek, M. H. (2012). Decomposition of European beech and Black pine foliar litter along an Alpine elevation gradient: mass loss and molecular characteristics. Geoderma, 189, 522-531.

[5]   Fatai, A. A., Shamshuddin, J., Fauziah, C. I., Radziah, O., & Bohluli, M. (2017). Formation and characteristics of an Ultisol in Peninsular Malaysia utilized for oil palm production. Solid Earth, 60, 1-21.

[6]   Frazão, L. A., Paustian, K., Pellegrino Cerri, C. E., & Cerri, C. C. (2013). Soil carbon stocks and changes after oil palm introduction in the Brazilian Amazon. GCB Bioenergy, 5(4), 384390.

[7]   Friedlingstein, P., Jones, M. W., O'sullivan, M., Andrew, R. M., Hauck, J., Peters, G. P., ... & Zaehle, S. (2019). Global carbon budget 2019. Earth System Science Data, 11(4), 17831838.

[8]   Gasser, T., Crepin, L., Quilcaille, Y., Houghton, R. A., Ciais, P., & Obersteiner, M. (2020). Historical CO 2 emissions from land use and land cover change and their uncertainty. Biogeosciences, 17(15), 4075-4101.

[9]   Haberhauer, G., & Gerzabek, M. H. (1999). Drift and transmission FT-IR spectroscopy of forest soils: an approach to determine decomposition processes of forest litter. Vibrational Spectroscopy, 19(2), 413-417.

[10]   Hansen, S. B., Olsen, S. I., & Ujang, Z. (2014). Carbon balance impacts of land use changes related to the life cycle of Malaysian palm oil-derived biodiesel. The International Journal of Life Cycle Assessment, 19(3), 558-566.

[11]   Haron, K., Brookes, P., Anderson, J., & Zakaria, Z. (1998). Microbial biomass and soil organic matter dynamics in oil palm (Elaeis guineensis Jacq.) plantations, West Malaysia. Soil Biology and Biochemistry, 30(5), 547-552.

[12]   Heiri, O., Lotter, A. F., & Lemcke, G. (2001). Loss on ignition as a method for estimating organic and carbonate content in sediments: reproducibility and comparability of results. Journal of paleolimnology, 25(1), 101-110.

[13]   Helfrich, M., Ludwig, B., Buurman, P., & Flessa, H. (2006). Effect of land use on the composition of soil organic matter in density and aggregate fractions as revealed by solid-state 13C NMR spectroscopy. Geoderma, 136(1-2), 331-341.

[14]   Jafarzadeh-Haghighi, A. H., Shamshuddin, J., Hamdan, J., Zainuddin, N., & Roslan, I. (2015). Carbon contents and structural characteristics of organic matter in soils of a climobiosequence in the Main Range of

Peninsular Malaysia. Asian Journal of Agriculture and Food Sciences (ISSN: 2321–1571), 3(05).

[15] Jusop, S., Paramananthan, S., & Wan, N. M. N. (1979). Soil Map of the Universiti Pertanian Malaysia Farm. Soil Science Department, Universiti Pertanian Malaysia.

[16] Kleber, M., Sollins, P., & Sutton, R. (2007). A conceptual model of organo-mineral interactions in soils: self-assembly of organic molecular fragments into zonal structures on mineral surfaces. Biogeochemistry, 85(1), 9-24.

[17] Lu, X., Gilliam, F. S., Guo, J., Hou, E., & Kuang, Y. (2022). Decrease in soil pH has greater effects than increase in above ground carbon inputs on soil organic carbon in terrestrial ecosystems of China under nitrogen enrichment. Journal of Applied Ecology, 59(3), 768778.of China under nitrogen enrichment. Journal Of Applied Ecology.

[18] MacCarthy, P & Rice, J. A. (1985). Spectroscopic Methods (Other than NMR) for Determining Functionality in Humic Substances. In Humic Substances in Soil, Sedimen, and Water: Geochemistry, Isolation and Characerization; Aiken, G., McKnight, D., Wershaw, R., Eds.; John Wiley & Sons: New York; Chapter 21, pp 527-559.

[19] Margenot, A. J., Calderón, F. J., Bowles, T. M., Parikh, S. J., & Jackson, L. E. (2015). Soil organic matter functional group composition in relation to organic carbon, nitrogen, and phosphorus fractions in organically managed tomato fields. Soil Science Society of America Journal, 79(3), 772-782.

[20] Nguyen, T. T., Janik, L. J., & Raupach, M. (1991). Diffuse reflectance infrared Fourier transform (DRIFT) spectroscopy in soil studies. Soil Research, 29(1), 49-67.

[21] Pansu, M., & Gautheyrou, J. (2007). Handbook of soil analysis: mineralogical, organic and inorganic methods. Springer Science & Business Media.

[22] Pisani, O., Hills, K. M., Courtier-Murias, D., Haddix, M. L., Paul, E. A., Conant, R. T., Simpson, A ., Arhonditsis , G & Simpson, M. J. (2014). Accumulation of aliphatic compounds in soil with increasing mean annual temperature. Organic Geochemistry, 76, 118-127.

[23] Rumpel, C., Kögel-Knabner, I., & Bruhn, F. (2002). Vertical distribution, age, and chemical composition of organic carbon in two

forest soils of different pedogenesis. Organic Geochemistry, 33(10), 1131-1142.

[24] Tatzber, M., Mutsch, F., Mentler, A., Leitgeb, E., Englisch, M., Zehetner, F., Djukic, I & Gerzabek, M. H. (2011). Mid-infrared spectroscopy for topsoil layer identification according to litter type and decompositional stage demonstrated on a large sample set of Austrian forest soils. Geoderma, 166(1), 162-170.

[25] Wang, J., Bai, J., Zhao, Q., Lu, Q., & Xia, Z. (2016). Five-year changes in soil organic carbon and total nitrogen in coastal wetlands affected by flow-sediment regulation in a Chinese delta. Scientific Reports, 6, 21137.

[26] Yu, H., Ding, W., Chen, Z., Zhang, H., Luo, J., & Bolan, N. (2015). Accumulation of organic C components in soil and aggregates. Scientific Reports, 5(1), 1-12.

[27] Zhu, X., Chen, H., Zhang, W., Huang, J., Fu, S., Liu, Z., & Mo, J. (2016). Effects of nitrogen addition on litter decomposition and nutrient release in two tropical plantations with N2fixing vs. non-N2-fixing tree species. Plant and Soil, 399(1-2), 61-74.

[28] Zulkifli, S. Z., Mohamat-Yusuff, F., Mukhtar, A., Ismail, A., & Miyazaki, N. (2014). Determination of food web in intertidal mudflat of tropical mangrove ecosystem using stable isotope markers: A preliminary study. Life Science Journal, 11(3), 427-431.**s**